

Core-Collapse Very Massive Stars: Evolution, Explosion, and Nucleosynthesis of Population III 500 – 1000 M_{\odot} Stars

Takuya Ohkubo¹, Hideyuki Umeda¹, Keiichi Maeda², Ken'ichi Nomoto^{1,3}, Tomoharu Suzuki¹, Sachiko Tsuruta⁴, and Martin J. Rees⁵

ABSTRACT

We calculate evolution, collapse, explosion, and nucleosynthesis of Population III very-massive stars with $500M_{\odot}$ and $1000M_{\odot}$. Presupernova evolution is calculated in spherical symmetry. Collapse and explosion are calculated by a two-dimensional code, based on the bipolar jet models. We compare the results of nucleosynthesis with the abundance patterns of intracluster matter, hot gases in M82, and extremely metal-poor stars in the Galactic halo. It was found that both $500M_{\odot}$ and $1000M_{\odot}$ models enter the region of pair-instability but continue to undergo core collapse. In the presupernova stage, silicon burning regions occupy a large fraction, more than 20% of the total mass. For moderately aspherical explosions, the patterns of nucleosynthesis match the observational data of both intracluster medium and M82. Our results suggest that explosions of Population III core-collapse very-massive stars contribute significantly to the chemical evolution of gases in clusters of galaxies. For Galactic halo stars, our [O/Fe] ratios are smaller than the observational abundances. However, our proposed scenario is naturally consistent with this outcome. The final black hole masses are $\sim 230M_{\odot}$ and $\sim 500M_{\odot}$ for the $500M_{\odot}$ and $1000M_{\odot}$ models, respectively. This result may support the view that Population III very massive

¹Department of Astronomy, School of Science, University of Tokyo, 7-3-1 Hongo, Bunkyo-ku, Tokyo 113-0033, Japan; ohkubo@astron.s.u-tokyo.ac.jp, umeda@astron.s.u-tokyo.ac.jp, nomoto@astron.s.u-tokyo.ac.jp, suzuki@astron.s.u-tokyo.ac.jp

²Department of Earth Science and Astronomy, graduate school of Arts and Sciences, University of Tokyo, 3-8-1, Komaba, Meguro-ku, Tokyo 153-8902, Japan; maeda@esa.c.u-tokyo.ac.jp

³Research Center for the Early Universe, School of Science, University of Tokyo, 7-3-1 Hongo, Bunkyo-ku, Tokyo 113-0033, Japan

⁴Department of Physics, Montana State University, Bozeman, MT 59717-3840; uphst@gemini.msu.montana.edu

⁵Institute of Astronomy, Cambridge University, Madingley Road, Cambridge CB3 0HA, UK; mjr@ast.cam.ac.uk

stars are responsible for the origin of intermediate mass black holes which were recently reported to be discovered.

Subject headings: nuclear reactions, nucleosynthesis, abundances – stars: evolution – stars: supernovae: general – stars: abundances – galaxies: starburst – galaxies: intergalactic medium

1. Introduction

One of the most interesting challenges in astronomy is to investigate the mass and properties of first generation "Population III (Pop III)" stars, and how various elements have been synthesized in the early universe. Just after the Big Bang these elements were mostly only H, He and a small amount of light elements (Li, Be, B, etc). Heavier elements, such as C, O, Ne, Mg, Si and Fe, were synthesized during the evolution of later generation stars, and massive stars exploded as supernovae (SNe), releasing heavy elements into space.

Stars end their lives differently depending on their initial masses M . Here the Pop III stars are assumed to undergo too little mass loss to affect the later core evolution. Then the fates of Pop III stars are summarized as follows. Those stars lighter than $8M_{\odot}$ form white dwarfs. Those with $8M_{\odot} - 130M_{\odot}$ undergo ONe-Fe core collapse at a last stage of their evolution leaving neutron stars or black holes. Some of these stars explode as the core-collapse supernovae. Stars with $130M_{\odot} - 300M_{\odot}$ undergo electron-positron pair creation instability during oxygen burning, releasing more energy by nuclear burning than the gravitational binding energy of the whole star, and hence these stars disrupt completely as the pair-instability supernovae (PISN). Stars with $300M_{\odot} - 10^5M_{\odot}$ also enter into the pair-instability region but continue to collapse. Fryer, Woosley, & Heger (2001) calculated evolution of 260 and 300 M_{\odot} stars and obtained the result that a 260 M_{\odot} star ends up as a PISN and a 300 M_{\odot} star collapsed. Stars over $\sim 10^5M_{\odot}$ collapse owing to general relativistic instability before reaching the main-sequence. The core collapse SNe (Type II, Ib and Ic SNe) release mainly α -elements such as O, Mg, Si and Ca and some Fe-peak elements as well.

It has been suggested that the initial mass function (IMF) of Pop III first stars may be different from the present one - that more massive stars existed in the early universe (e.g., Nakamura & Umemura 1999; Abel, Bryan, & Norman 2000; Bromm, Coppi, & Larson 2002; Omukai & Palla 2003). Some authors (e.g., Wasserburg and Qian 2000; Qian, Sargent, Wasserburg 2002; Qian and Wasserburg 2002; & Yoshida et al. 2004) argued that existence of very massive stars (VMSs) in the early universe is consistent with abundance data of Ly α

systems. Numerical simulations by, e.g., Bromm & Loeb (2004), indicate that the maximum mass of Pop III stars to be formed will be $\sim 300M_{\odot} - 500M_{\odot}$. Omukai & Palla (2003), however, point out that under certain conditions VMSs much heavier than $300M_{\odot}$ can be formed in the zero-metallicity environment. Tan & McKee (2004) calculated star formation by taking rotation and disk structure and concluded that first stars should be much more massive than $30M_{\odot}$. Another scenario for the formation of VMSs for any metallicity has been presented by Ebisuzaki et al. (2001) and Portegies Zwart et al. (1999, 2004a, 2004b), where VMSs are formed by merging of less massive stars in the environment of very dense star clusters.

In the present paper, we call the stars with $M \gtrsim 10^5 M_{\odot}$ "Super-Massive Stars (SMSs)", and the stars with $M = 130M_{\odot} - 10^5 M_{\odot}$ "Very-Massive Stars (VMSs)". Among "VMSs" we define $M > 300M_{\odot}$ stars as "Core-Collapse Very-Massive Stars (CVMSs)", in order to clarify the distinction between the PISN mass range and the core-collapse range. Here we focus on CVMSs, and deal with 500 and 1000 M_{\odot} models.

Such CVMSs might have released a large amount of heavy elements into space by mass loss and/or supernova explosions, and they might have significantly contributed to the early galactic chemical evolution, if they were the source of reionization of intergalactic H and He (e.g., Gnedin & Ostriker 1997; Venkatesan, Tumlinson, & Shull 2003). The reionization of intergalactic He has traditionally been attributed to quasars. However, according to the results of the *the Wilkinson Microwave Anisotropy Probe* (WMAP) observation in 2003, reionization in the universe took place as early as 0.2-0.3 billion years after the Big Bang (redshift $z \gtrsim 20$) (Kogut et al. 2003). Then these Pop III CVMSs might provide a better alternative channel which could operate at redshifts higher than what is assumed for quasars (Bromm, Kudritzki, & Loeb 2001).

The question of whether CVMSs ($\sim 300M_{\odot} - 10^5 M_{\odot}$) actually existed is of great importance, for instance, to understand the origin of intermediate mass black holes (IMBHs) ($\sim 5 \times 10^{(2-4)} M_{\odot}$). Stellar mass black holes ($\sim 10M_{\odot}$) are formed as the central compact remnants of ordinary massive ($25 - 130M_{\odot}$) stars at the end of their evolution, while super-massive black holes (SMBHs) ($\sim 10^5 - 10^9 M_{\odot}$) are now known to exist in the center of almost all galaxies (e.g., Kormendy & Richstone 1995; Bender 2004). IMBHs have not been found until recently. However, there is a strong possibility that some IMBHs have been, indeed, found (e.g., Barth, Green, & Ho 2005 for most recent review). Matsumoto et al. (2001) reported possible identification of a $\gtrsim 700M_{\odot}$ black hole in M82, by using *Chandra* data. As to formation of SMBHs there are several scenarios (e.g., Rees 2002, 2003). SMBHs may be formed directly from supermassive halos of dark matter (e.g., Marchant & Shapiro 1980; Bromm and Loeb 2003). Ebisuzaki et al. (2001) suggested a scenario where IMBHs grow to

a SMBH by merging and swallowing of many of these objects. If CVMSs actually existed, they could be considered as natural progenitors of IMBHs.

Motivated by these backgrounds, here we calculate the evolution, collapse, explosion, and nucleosynthesis of Pop III CVMSs (over $300M_{\odot}$). These stars are expected to form black holes directly at the end of evolution. It has not been known yet if they will explode as SNe. However, if the star is rotating the whole star will not become a black hole at once, but it is expected to form an accretion disk around the central remnant (e.g. Shibata & Shapiro 2002). After forming an accretion disk, jet-like explosions may occur by extracting energy from the accretion disk and/or the black hole itself (Fryer et al. 2001; MacFadyen et al. 2001; Maeda & Nomoto 2003). Therefore, in our current explosion and collapse calculations we adopt a two-dimensional approach including accretion along the equatorial direction and jets toward the polar direction.

We compare our results of nucleosynthesis with the observed abundance data of intra-cluster medium (ICM), intergalactic medium (IGM), gases in the central part of M82, and extremely metal-poor (EMP) stars in the Galactic halo. Since it is very difficult to observe directly the explosions of the first generation stars due to the large distance (redshift $z \gtrsim 20$), currently *comparison of the kind carried out in this study will offer a powerful method to support the existence of such very massive stars.*

After describing the basic methods adopted and the assumptions made for our models in section 2, the results are presented and discussed in section 3, and they are compared with observations in section 4. Further discussion and concluding remarks are given in the last section, section 5.

2. Methods, Assumptions & Models

We calculate evolution, core collapse, explosion, and nucleosynthesis of very-massive stars with $500M_{\odot}$ and $1000M_{\odot}$. As mentioned in Introduction, such massive stars may be formed in a metal-free environment. We start our evolutionary calculations by assuming that the stars have 500 and $1000M_{\odot}$, with zero-metallicity, on the pre-main sequence. As our starting approximation we neglect radiative mass loss due to zero metallicity (Kudritzki 2000). Ibrahim et al. (1981), Baraffe et al. (2001), and Nomoto et al. (2003) showed that pulsational mass loss is not so effective for metal-free stars, so we also neglect the pulsational mass loss. To calculate presupernova evolution we adopt the stellar evolution code constructed by Umeda & Nomoto (2002) based on the Henyey method. This code is developed from the codes constructed by Nomoto & Hashimoto (1988), and Umeda et al. (1999).

The nuclear reaction network for calculating nucleosynthesis and energy generation at each stage of the evolution is developed by Hix & Thielemann (1996). We include 51 isotopes up to Si until He burning ends, and 240 up to Ge afterwards. Our evolutionary calculations are carried out from the pre-main sequence up to the iron-core collapse where the central density reaches as high as $2 \times 10^{10} \text{gcm}^{-3}$. When the temperature reaches $5 \times 10^9 \text{K}$, where ”nuclear statistical equilibrium” (NSE hereafter) is realized, the abundance of each isotope is determined for a given set of density, temperature, and Y_e . Here Y_e is the number of electrons per nucleon, defined as:

$$Y_e = \sum_i \frac{Z_i}{A_i} X_i. \quad (1)$$

where Z_i is the atomic number, A_i is the mass number, and X_i is the mass fraction of species i . Y_e , as well as density and temperature, is a key quantity to determine the abundance of each element. We assume NSE at $\log T \text{ (K)} \geq 9.7$.

The explosion mechanism of core-collapse supernovae is not well understood. Moreover, we do not know beforehand how very massive stars over $300M_\odot$ explode due to strong gravitation even when they are rotating. In this study, therefore, instead of going into the problem of whether such massive stars actually explode, we investigate the conditions required for these stars to explode, by exploring several situations with various models. For the explosion in the hydrodynamical simulation, we adopt the two-dimensional (2D) Newtonian hydrodynamical code constructed by Maeda & Nomoto (2003) and Maeda (2004). This code adopts the Eulerian coordinate and solves Euler equations based on Roe’s scheme (Hachisu et al. 1992, 1994). Previously 2D simulations of jet-induced supernova explosions have been carried out by many authors for ordinary massive stars with $\sim 25M_\odot$ to $40M_\odot$ (Khokhlov et al. 1999; MacFadyen et al. 2001; Nagataki 2000; Maeda et al. 2002; Maeda & Nomoto 2003; Maeda et al. 2006). However, there have been no such detailed calculations for CVMSs with $M \gtrsim 500M_\odot$. Because temperatures are so high at the explosion, the pressure is radiation-dominated, and hence we use the equation of state for the radiation and electron-positron pairs with the adiabatic index of $4/3$.

The explosion models to be explored are summarized in Tables 1 and 2. Jets, which are supposed to be injected from the accretion disk, are considered to be the energy source of the explosion. We first choose the initial black hole mass, and the outer matter accretes toward the central object. Because our hydrodynamical code includes gravitational force, the final black hole mass and the ejected mass are determined as the results of the calculations for a set of given parameters (Maeda & Nomoto 2003). One of the purposes of this study is to explore the condition for the stars to explode when jets are injected. As typical cases we choose the initial black hole mass, M_{BH0} , at $100M_\odot$ for the $1000M_\odot$ star and $50M_\odot$ for the

$500M_{\odot}$ star. However, in order to investigate the dependence of results on this parameter, we also explore larger or smaller values of M_{BH0} .

We adopt the spherical polar coordinate with the number of meshes set to 150×60 for five models (higher resolution; A-1, A-2, B-1, B-2, and B-3), and 100×30 for the rest (lower resolution). The latter models are chosen so that we can search for parameter dependence quickly. We describe our results mainly based on those of higher resolution models. However, we include lower resolution models to explore the detailed dependence on parameters. We also calculate Model B-2 with lower resolution, in order to numerically compare the two resolutions. The difference of the quantities we give in Tables 3, 4, 6, and 7 between the two resolutions is around 10 %.

At the beginning of hydrodynamical simulations, the region $M_{\text{BH0}} < M_r$ is mapped onto the computational domain. The central part ($M_r \leq M_{\text{BH0}}$) is displaced by a point mass. The inner boundary of the simulations is set at the radius R_0 (see Tables 1 and 2). In the computational domain, we assume that the effect of rotation is negligible. This assumption applies if the specific angular momentum $j_{17} = j/10^{17} \text{ cm}^2 \text{ s}^{-1}$ in the progenitor star is in the range $6.3 \leq j_{17} < 45$, where the lower and upper limits correspond to the conditions that the disk forms beyond the schwarzschild radius and well below the inner boundary of our computational domain. If $j_{17} \sim 6.3$, which is favorable in order to make an efficiently accreting disk (Narayan, Piran, & Kumer 2001), then the rotational force is at most a few percent of the gravitational force at the inner boundary.

For the jet injection, we choose various values for the parameter, θ_{jet} , the angle from the polar axis. The jet is injected into the direction of $0 \leq \theta \leq \theta_{\text{jet}}$. At the direction $\theta > \theta_{\text{jet}}$, the inner boundary is treated as follows: it is set to be transmitted (absorbed; i.e., vanishing radial gradient of all variables) or reflected if the material just above the boundary has negative (accreting) or positive sign. These boundary conditions are used in previous studies on jet-induced supernova explosions (Khokhlov et al. 1999; Macfadyen, Woosley, & Heger 2001, Maeda & Nomoto 2003). It should be noted that by using the transmitted boundary condition for the accretion case and neglecting pressure and rotational support below the boundary, we may overestimate the accretion rate.

The energy and mass injected by the jets per unit time are connected with the properties of accreting matter as (Maeda & Nomoto 2003):

$$\dot{E}_{\text{jet}} = \epsilon \dot{M}_{\text{acc}} c^2 = \dot{E}_{\text{thermal}} + \left(\frac{1}{2} \rho_{\text{jet}} v_{\text{jet}}^2\right) v_{\text{jet}} A_{\text{jet}} \quad (2)$$

$$\dot{M}_{\text{jet}} = \mu \dot{M}_{\text{acc}} = \rho_{\text{jet}} v_{\text{jet}} A_{\text{jet}} \quad (3)$$

where \dot{M}_{acc} is the accretion rate, \dot{E}_{jet} the injected energy per unit time, \dot{M}_{jet} the mass spouted per unit time, ϵ the energy transformation efficiency, μ the mass fraction of the jets to the

accreted matter, ρ_{jet} the jet density, v_{jet} the jet velocity, and A_{jet} the area over which the jet is spouted, respectively. We treat ϵ and μ as free parameters to be varied to explore the explosion energy.

We consider two cases for the form of the injected energy. One is that almost all the energy of the jet is given as kinetic energy (Case A). The other is that almost all the energy is given as thermal energy (Case B). We introduce a parameter F_{thermal} defined as:

$$F_{\text{thermal}} = \frac{\dot{E}_{\text{thermal}}}{\dot{E}_{\text{jet}}} \quad (4)$$

i.e., the ratio of thermal energy in the jet to the total jet energy per unit time. This parameter is set to 0.01 for Case A, and to 0.9 or 0.95 for Case B. By using equations 2, 3 and 4 we obtain the jet velocity:

$$v_{\text{jet}} = \left[\frac{2\epsilon(1 - F_{\text{thermal}})}{\mu} \right]^{1/2} c. \quad (5)$$

Equations 2,3, and 4 give a complete set of jet properties at the inner boundary. In Case A the jet carries most energy toward the polar (jet-injected) direction, and hence the model is highly non-spherical. For this case, we set the ratio between the two parameters, ϵ/μ , to 0.1. Because we perform a Newtonian calculation, the larger we set ϵ the larger we need to set μ , so that the jet material does not exceed or approach the speed of light. For Case B, on the other hand, the models, due to the dominant thermal energy, become more spherical, because thermal motion is random and non-directional. For this case, we set larger ϵ values for the same μ compared with Case A. This means that the jet is something like a hot bubble.

One of our primary purposes is to investigate how much heavy elements are synthesized and ejected by the explosion. Therefore we stop the calculations when all of the following conditions are satisfied:

- 1 \dot{M}_{acc} decreases enough below $0.1M_{\odot} \text{ s}^{-1}$, i.e., $\lesssim 0.02M_{\odot} \text{ s}^{-1}$.
- 2 Total explosion energy E_{tot} becomes much larger than the absolute gravitational binding energy $|E_{\text{grav}}|$, $E_{\text{tot}} \gtrsim 10|E_{\text{grav}}|$.
These criteria mean that accretion has almost stopped.
- 3 The maximum temperature of the matter decreases below $8 \times 10^8 \text{ K}$.
This means that explosive nucleosynthesis no longer occurs at such low temperatures.

Under these criteria, calculations sometimes end before jets reach the stellar surface.

Maeda & Nomoto (2003) used helium stars (the hydrogen envelope is removed by mass loss) as the initial models, and carried out the calculations for about 100 s until the jet reaches the stellar surface and the expansion becomes homologous. In contrast the radii of the stars we use here are in the order of $10^2 R_\odot$ ($\sim 10^{13}$ cm) because they have the hydrogen-rich envelope. Because we investigate the first generation stars, the mass loss will not be effective due to the metal-free environment. Therefore, it is reasonable to examine a hydrogen-rich star rather than a He star.

We calculated explosive nucleosynthesis by using temporal histories of density and temperature stored during hydrodynamical calculations. The reaction network we use includes 280 isotopes up to ^{79}Br . At high temperatures, $T_9 = T/10^9 \text{ K} > 5$, NSE is realized. We use the "NSE" code (Hix & Thielemann 1996) for $T_9 > 6$.

The jet matter should be included in the ejected matter and we need to calculate its nucleosynthesis. We do not know which of the accreted matter is injected as jets, and so the final chemical composition is uncertain. However, Pruet et al. (2004) carried out nucleosynthesis of disk wind for various Y_e values. MacFadyen & Woosley (1999) and MacFadyen (2003) also considered disk wind. Based on these works in this study we make the following assumptions:

- 1 Because the jet matter is injected through the inner region (from the accretion disk), it should have experienced high temperatures at which NSE is realized ($T_9 > 5$).
- 2 The jet matter expands adiabatically after it is injected (i.e., entropy is conserved).
- 3 The accreted matter is mostly accreted while the accretion rate \dot{M}_{acc} is of the order of $10 - 10^2 M_\odot \text{ s}^{-1}$. It is likely that ρ varies depending on when the jet material is injected. Therefore s (entropy density, $\propto \frac{T^3}{\rho}$) is likely to vary as well.
- 4 For the value of Y_e we assume $0.48 \leq Y_e \leq 0.52$.

Based on these assumptions we start the calculation of nucleosynthesis of the jet matter from $T_9 = 6$, using the historical temperature and density data of the first test particle of the jet (injected at the first stage of the explosion) in Model A-2 (history A), and the changed entropy data (double (history B) or triple (history C) the density at the same temperature). In other words, we use three ρ – T histories (history A: $(\rho(t), T(t))$, history B: $(2\rho(t), T(t))$, and history C: $(3\rho(t), T(t))$), where the set $(\rho(t), T(t))$ is given by the hydrodynamic simulations. Y_e is parameterized at 0.48, 0.49, 0.50, 0.51, and 0.52. We calculate 15 patterns and average these results to the first approximation. Y_e and entropy of the jet material can change when it is ejected. Therefore here we consider combination of jets with different values of these

parameters. These assumptions still include large uncertainty, but our aim is just to roughly estimate the amount of ^{56}Ni . The larger the mass of the jet is, the larger we expect the uncertainties to be.

3. Results

3.1. Presupernova Evolution

3.1.1. Evolutionary Tracks

Figure 1 shows the evolutionary tracks of the central density - temperature relation for $500M_{\odot}$ and $1000M_{\odot}$ stars. We also plot, for comparison, the track of a $300M_{\odot}$ star, which results in the pair-instability supernova. Generally, more massive stars have higher entropies (lower densities) at the same temperatures (i.e., at the same burning stage). Although each star passes through the region of electron-positron pair-instability, both $500M_{\odot}$ and $1000M_{\odot}$ stars proceed to iron-core collapse (Fe-decomposition region in Figure 1), unlike the $300M_{\odot}$ star. The $500M_{\odot}$ and $1000M_{\odot}$ stars do not become pair-instability supernovae though they pass through the pair-instability region, because the energy released at this stage is less than the gravitational binding energy of the star (Rakavy et al. 1967; Bond et al. 1984; Glatzel et al. 1985; Woosley 1986).

3.1.2. Presupernova Model

Figure 2 shows the presupernova chemical composition for the $500M_{\odot}$ and $1000M_{\odot}$ stars. In the region labeled as "NSE region", NSE is realized. For this region, we calculate the evolutionary changes in terms of (Y_e, ρ, T) to obtain the NSE abundances. One can see the onion-like structure from the center to the surface - the iron-core, silicon layer, oxygen layer, helium layer, and hydrogen-rich layer. Here we define the iron-core as the region where the mass fraction of Si is less than 10%. The iron-core occupies up to $130M_{\odot}$ of mass from the center for the $500M_{\odot}$ star, and $250M_{\odot}$ for the $1000M_{\odot}$ star. For both cases, they occupy a quarter of the total mass. This fraction is much larger than that in ordinary massive stars. For example, in a $25M_{\odot}$ star, the iron-core is about $1.6M_{\odot}$ (Umeda et al. 1999), less than 10% of the total mass. The reason is the difference of the density and temperature structure.

Figure 3 shows the density and temperature structure of the two stars just before the explosion (when the central density reaches $10^{10} \text{ g cm}^{-3}$), which is compared with the $25M_{\odot}$ model. The density and temperature gradients for the $500M_{\odot}$ and $1000M_{\odot}$ stars are smaller

than those of the $25M_{\odot}$ star, and hence the regions with high temperature and high density are larger. Then the fraction of the iron-core is larger. The large drop of density at $M_r/M_{\text{total}} \sim 0.5$ for the $500M_{\odot}$ and $1000M_{\odot}$ stars in Figure 3 corresponds to the boundary between the oxygen and helium layer.

3.2. Explosion Hydrodynamics

We describe the results of explosion hydrodynamics in this subsection and nucleosynthesis in the next subsection, showing several figures. All figures are based on the results of high resolution models, except for Figure 4.

3.2.1. Explosion Energy and Ejected Mass

In Tables 3 and 4 we summarize for each model the total explosion energy, final black hole mass, and mass of the jets. The total explosion energy is of the order of 10^{54} erg for most cases, except that in Model A-4 it is of the order of 10^{53} erg. Model A-4 is almost at the border between the ‘successful’ and ‘failed’ explosions. Actually, we also try to calculate the case which has the same parameters as Model A-4 except that ϵ and μ are half the values of A-4 (see Model F-1 in Table 5), but in this model the jet promptly falls back to the central remnant after it is injected, and hence the explosion fails. In this model, the total energy is still negative and the stellar matter moves toward the central remnant more than 200 s after the beginning of the accretion. The absolute value of gravitational binding energy over the region outside of the central $100M_{\odot}$ core is as high as 10^{55} ergs for the $1000M_{\odot}$ model. In this case energy injection is too weak for the jet to proceed outward.

Table 5 summarizes the models in which explosion ends up as ‘failure’. Figure 4 shows the models in which the explosion either occurs or not, depending on the two parameters θ_{jet} and ϵ . One can see that the minimum ϵ needed for the successful explosion becomes higher if θ_{jet} is larger, as in Model A-2 and Case B (most of the injected energy is given as thermal energy). Actually, explosion energies tend to be lower in such models than those in Case A models with $\theta_{\text{jet}} = 15^\circ$. In Model A-2 and Case B models, the injected energy tends to diffuse into the direction apart from the polar direction, and so the jet is weak even for the polar direction.

Figure 5 shows how the jet is propagating through the star by plotting the density structures. One can see that the jet is strongly propagating in the polar direction for A-1, while for B-1 the jet is broadened toward the side directions due to the random heat motion.

The final black hole mass and ejected mass are also important. For the $500 M_\odot$ and the $1000 M_\odot$ models, these values are $\sim 230 M_\odot$ and $500 M_\odot$, respectively.

3.2.2. Direction-Dependent Features

Figure 6 shows the regions where the matter will be accreted onto the central black hole. In these figures we can see the extent of asphericity and the amount of accreting matter. These panels show the initial positions (just before the explosion) of the accreted matter. In Model A-2 in which θ_{jet} is twice (30°) the other models (15°) and Case B, asphericity is weakened to some extent and the amount of the accreting matter is less compared with the models with $\theta_{\text{jet}} = 15^\circ$ and the same energy transformation efficiency ϵ . For models with $\theta_{\text{jet}} = 15^\circ$, the stellar matter toward the direction $\theta > \theta_{\text{jet}}$ almost accretes up to $500 M_\odot$ (even a part of the helium layer) on the mass coordinate. On the other hand, in Model A-2 and Case B models a large amount of matter inner than the $500 M_\odot$ core is ejected. At the same time, if asphericity becomes weaker the threshold efficiency for the successful explosion becomes more strict— that is, larger ϵ is needed. This is because more energy diffuses toward the equatorial direction.

In Figure 7 we show the maximum temperatures which each mesh reaches and the densities at the maximum temperatures for the z (polar)-direction, $\theta = 15^\circ, \theta = 45^\circ$. We may pay special attention to the maximum T_9 for the $\theta = 15^\circ$ and $\theta = 45^\circ$ direction. For some models (e.g., A-1 in the left panel) with $\theta_{\text{jet}} = 45^\circ$, the maximum T_9 does not appear within the range of these graphs, because the matter which can experience such high temperatures is in the inner region, and hence such matter all accretes in these models. However, for the other cases, the inner matter is ejected and the explosive nucleosynthesis occurs even for the $\theta = 45^\circ$ direction.

3.3. Explosive Nucleosynthesis

When a shock arrives the shocked region is compressed and heated, drastically raising the density and temperature, and then the explosive nucleosynthesis occurs. The products of this event are characterized by the peak temperature. We first summarize the main products at different peak temperatures and then describe the results of the calculations.

3.3.1. Explosive Burning and Products

If the peak temperature T_{peak} exceeds 5×10^9 K, NSE is realized. In such regions ‘complete silicon burning’ occurs and then Fe-group elements (such as Mn, Co, Fe, Ni) are produced. The main product is ^{56}Ni , which eventually decays into ^{56}Fe .

In the complete silicon burning region, at lower density for a given temperature the reaction rate decreases, and the number of free-particles may exceed the NSE value. Or, if the initial temperature is higher, free-particles become more abundant because in NSE the number of these particles is a high-powered function of temperature. This situation is called ‘ α -rich freezeout’, and it tends to produce the Fe-group elements and nuclei to the high-Z side of the peak (e.g. Thielemann, Nomoto, & Hashimoto 1996; Arnett 1996).

If $4 \times 10^9\text{K} < T_{\text{peak}} < 5 \times 10^9\text{K}$, *incomplete Si burning* occurs. In such regions, Si is not all converted into the Fe-group elements but remains or is converted to the elements such as ^{32}S , ^{36}Ar , and ^{40}Ca .

If $3 \times 10^9\text{K} < T_{\text{peak}} < 4 \times 10^9\text{K}$, *explosive oxygen burning* occurs, which produces ^{28}Si and ^{32}S , while the original ^{16}O composition stays the same.

If $2 \times 10^9\text{K} < T_{\text{peak}} < 3 \times 10^9\text{K}$, *explosive carbon burning* occurs, which produces ^{20}Ne and ^{24}Mg . The original ^{12}C remains because the burning does not proceed during such a short time scale.

If $T_{\text{peak}} < 2 \times 10^9\text{K}$, almost no explosive burning occurs, and so the original chemical composition realized during the hydrostatical burning phase is conserved.

3.3.2. Direction-Dependent Features

As typical interesting cases, Figures 8 – 10 show the distribution of elements after the explosive nucleosynthesis for Models A-1, A-2 and B-1, respectively. In each figure the upper left panel shows the Fe-group elements in the polar direction. The upper right panel shows the α - elements in the polar direction, the lower left panel shows the α - elements at $\theta = 15^\circ$, and the lower right panel shows the α - elements at $\theta = 45^\circ$. In each model, complete silicon burning region shows strong α -rich freezeout. The upper panel (polar direction) in each figure shows that ^{56}Ni is synthesized dominantly up to $400M_\odot$ from the center. Compared with Figure 2 which shows the chemical composition just before the explosion, one can see that oxygen is consumed in the region with $350 - 400 M_\odot$.

For directions $\theta = 15^\circ$ and $\theta = 45^\circ$ the silicon and oxygen layers considerably accrete,

and even a part of the helium layer accretes for $\theta = 45^\circ$ for Model A-1. On the other hand, in Models A-2 and B-1 the complete silicon burning region still remains for $\theta = 15^\circ$ and the oxygen layer remains for $\theta = 45^\circ$. This is because the shock is diffused to the equatorial directions more than Model A-1.

Figure 11 shows the mass fractions of ^{56}Ni and α -elements for each θ integrated over the radial direction. These figures clearly show how much matter is ejected - for example, the ejected mass of the oxygen layer by seeing the mass fraction of ^{16}O . For the $\theta_{\text{jet}} = 15^\circ$ models in Case A (e.g., A-1) there is no ejected matter except helium and hydrogen in the directions $\theta > 45^\circ$ (see also Figure 8). However, for Case B and the $\theta_{\text{jet}} = 30^\circ$ models of Case A (e.g., A-2 or B-1) the ^{56}Ni synthesized region and α -element rich region are broadened to around $\theta = 30^\circ$ and 80° .

3.3.3. Composition of Jet Material

Figure 12 shows $[\text{X}/\text{Fe}]$ (top panel) and mass fractions (bottom panels) for the Fe-peak elements as a function of Y_e . Note that we assume the temperature of the jet material reaches higher than 5×10^9 K, and therefore it consists mostly of the Fe-group elements and ^4He .

Peculiar features are seen particularly when $Y_e < 0.5$. Co, Cu, Ni and Zn are dramatically abundant relative to Fe (500-1000 times larger than the solar values) as shown in Figure 12. When $Y_e < 0.5$ the mass fraction of synthesized ^{56}Ni is very small, less than 10% for $Y_e = 0.49$ and less than 0.1% for $Y_e = 0.48$. Then a large amount of neutron-rich nuclei, such as ^{58}Ni , ^{60}Ni , and ^{59}Ni (which decays into ^{59}Co), ^{63}Zn (which decays into ^{63}Cu), and ^{64}Zn , are synthesized. In these situations neutron-rich ^{64}Zn is directly synthesized rather than ^{64}Ge , which decays into ^{64}Zn . The rise of $[\text{Cr}/\text{Fe}]$ and $[\text{Mn}/\text{Fe}]$ for $Y_e < 0.5$ is mainly due to the small fraction of ^{56}Ni rather than the increase of the fractions of Cr and Mn.

On the other hand, for $Y_e > 0.5$ most of the products are ^{56}Ni and ^4He , similar to the case where $Y_e = 0.5$. The main effect of Y_e larger than 0.5 is the existence of free protons.

As our first step for the treatment of the jet material, Figure 13 shows the abundance pattern of jet material averaged over 15 patterns (5 Y_e values \times 3 entropy values). $[\text{Zn}/\text{Fe}]$ and $[\text{Ni}/\text{Fe}]$ are larger than the solar values due to the effects of small Y_e regions, while $[\text{Cr}/\text{Fe}]$ and $[\text{Mn}/\text{Fe}]$ are smaller due to the effects of large Y_e regions. The averaged mass fraction of ^{56}Ni is about 40%. We multiply the mass fraction of each nucleus by the jet mass and add it to the total abundance pattern.

3.4. Ionization Rates, Heavy Element Yield, and Ionization Efficiency

The suggestion that VMSs are responsible for the reionization of HI and HeI is not a new one (e.g., Gnedin & Ostriker 1997). Bromm, Kudritzki, & Loeb (2001) calculated the stellar atmosphere models for Pop III main-sequence CVMSs of 300 - 1000 M_{\odot} and obtained the effective temperatures of $\log T_{\text{eff}} \text{ (K)} \sim 5.05$, which are higher than $\log T_{\text{eff}} \text{ (K)} \sim 4.81$ of Pop I stars with the same mass and slightly higher than $\log T_{\text{eff}} \text{ (K)} = 4.85 - 5.0$ for Pop III 15 - 90 M_{\odot} stars (Tumlinson & Shull 2000). Thanks to the high effective temperature, Pop III CVMSs give high production rates of ionizing radiations $\sim 1.6 \times 10^{48} \text{ photons s}^{-1} M_{\odot}^{-1}$ for H I ionization, $1.1 \times 10^{48} \text{ photons s}^{-1} M_{\odot}^{-1}$ for He I ionization, and $3.8 \times 10^{47} \text{ photons s}^{-1} M_{\odot}^{-1}$ for He II ionization. These numbers correspond to ~ 16 , 14 and 75 times higher than the corresponding values with a Salpeter IMF (see Bromm et al. 2001), and therefore, they are sufficient for completely reionizing IGM.

Daigne et al. (2004) estimate the efficiency of supplying UV photons and chemical enrichment of IGM simultaneously. These authors suggest that the IMF that essentially forms less than 100 M_{\odot} is favorable. However, this conclusion is due to the assumption that all CVMSs collapse entirely to a black hole. Venkatesan & Truran (2003) considered the relation between the reionizing radiation and metal enrichment of IGM, using stellar atmosphere models and model yields available at that time. For the model yields, they assumed no metal ejection by stars of $\sim 30 - 130 M_{\odot}$ and also $M \gtrsim 300 M_{\odot}$. Following their argument, here we compute the reionization efficiency for our CVMSs using model yields in the present work.

Adopting the mass of heavy elements ejected by our 1000 M_{\odot} star model, $M_Z \sim 50 M_{\odot}$, the conversion efficiency (η_{Lyc}) of energy produced in the HI ionizing radiation divided by the energy produced in the rest mass of metals ($M_Z c^2$) is $\eta_{\text{Lyc}} \sim 0.05$. (We used Eq. 1 of Venkatesan & Truran 2003). Here we use the timescale of $t_{\text{ms}} = 2 \times 10^6$ years for the 1000 M_{\odot} Pop III star. With these values, the number of ionizing photons per baryon in the universe generated in association with the IGM metallicity $Z_{\text{IGM}} \sim 10^{-4}$, obtained for our model, is $N_{\text{Lyc}}/N_{\text{b}} \sim 150$. (We used Eq. 2 of Venkatesan & Truran 2003). Note that this value well exceeds the value required for reionization of inter galactic hydrogen, $1 < N_{\text{Lyc}}/N_{\text{b}} \lesssim 10$ (see Somerville et al. 2003). Therefore, contrary to the earlier results, our conclusion is that CVMSs can contribute significantly to reionization of IGM in the early epochs.

4. Integrated Abundance Patterns and Comparison with Observations

The abundance pattern, the mass ratio of each element to be compared with observations, is determined by integrating the distributions over the entire ejecta regions (both radial and θ directions). It is the mass ratio of each ejected element. Tables 6 and 7 show the ejected masses of some isotopes excluding the jet materials, and Table 8 shows the masses of all the isotopes including the jet materials.

4.1. Abundance Patterns without Jet Materials

Tables 6 and 7 show the ejected mass of ^{56}Ni (which decays into ^{56}Fe), excluding the jet material. Masses of ^{16}O and ^{28}Si are also shown as representative α -elements to see the abundance and ratios of these elements. In models for Case A (except Model A-4), the ratios of the ejected masses of these elements to their progenitor mass are rather small, compared with those ratios in ordinary massive stars such as a $25M_{\odot}$ star. The typical ejected ^{56}Ni mass in the $25M_{\odot}$ star is $\sim 0.1 M_{\odot}$ (Maeda & Nomoto 2003). In the models with $\theta_{\text{jet}} = 15^{\circ}$, asphericity is so strong that it is only toward small θ direction where ^{56}Ni and Fe-group elements are synthesized and ejected. On the other hand, in models for Case B and Model A-4, these masses are much larger than the other models. The ejected ^{56}Ni mass is about 5 - $10M_{\odot}$. If this kind of supernova occurs, it is very bright in its tail because the heating source of a supernova is γ -rays from radioactive decays of $^{56}\text{Ni} \rightarrow ^{56}\text{Co} \rightarrow ^{56}\text{Fe}$. However, it is very difficult to observe directly the explosions of first generation stars by present observational devices since they are very distant ($z \gtrsim 20$).

4.2. Total Abundance Pattern and Comparison with Observational Data

4.2.1. Intracluster Matter and Hot Gas in M82

Figure 14 and Figure 15 show the total abundance pattern for each model of higher resolution and lower resolution models, respectively, which is compared with the observational data of intracluster medium (ICM) and M82. Note that the following discussions do not depend on the resolution. In these figures the abundance data for the ICM gas are shown with the bars (Baumgartner et al. 2005; Peterson et al. 2003), while the pentagons show the data for the gas of the central region of M82 (Ranalli et al. 2005; see also Tsuru et al. 1997). These data show that (1) the ratio $[\text{O}/\text{Fe}]$ is smaller than the solar value, (2) $[\text{Ne}/\text{Fe}]$ is about the solar value, and (3) the intermediate-mass α -elements such as Mg, Si, S exhibit

oversolar abundance - that is, $[\text{Mg}/\text{Fe}]$, $[\text{Si}/\text{Fe}]$ and $[\text{S}/\text{Fe}] \sim 0.5$ (Origlia et al. 2004; Ranalli et al. 2005).

Note that these data are not explained by standard Type II SN nucleosynthesis models. Also, if underabundance of $[\text{O}/\text{Fe}]$ is due to the contribution of Type Ia SNe, other α -elements such as Si and S should be also underabundant. Loewenstein (2001) suggested the contribution of Pop III hypernovae (supernovae of ordinary massive stars such as $25M_{\odot}$, with the explosion energy of at least ~ 10 times larger than normal supernovae; e.g., Nomoto et al. 2003) to the enrichment of ICM, in order to explain low $[\text{O}/\text{Fe}]$ and high $[\text{Si}/\text{Fe}]$, using the hypernovae models by Nakamura et al. (2001) and Heger et al. (2001). Umeda et al. (2002) also discussed this feature, but they predicted smaller $[\text{Ne}/\text{Fe}]$ and $[\text{Mg}/\text{Fe}]$ than the data given by Ranalli et al. (2005).

Here we compare nucleosynthesis calculations of our CVMS models with these observational data. The results are summarized as follows. For our Case B models we obtain the abundance pattern generally close to the observations of both ICM and M82 - for instance, the underabundance of $[\text{O}/\text{Fe}]$ and $[\text{Ne}/\text{Fe}]$, and the over solar values of $[\text{Mg}/\text{Fe}]$, $[\text{Si}/\text{Fe}]$ and $[\text{S}/\text{Fe}]$. On the other hand, all Case A models result in very underabundant values of $[\alpha/\text{Fe}] \lesssim -1$ because the mass fraction of ^{56}Ni synthesized in the jet matter is much larger than that synthesized in the matter which does not accrete. What is more, contribution by the jet material is dominant in such models and the uncertainty is very large. The yields of PISNe (Heger & Woosley 2002; Umeda & Nomoto 2002) are $[\text{O}/\text{Fe}] \sim [\text{Mg}/\text{Fe}]$, $[\text{Ne}/\text{Fe}] \sim 0$, and $[\text{Si}/\text{Fe}]$ and $[\text{S}/\text{Fe}] \sim 1.0$, not consistent with these data. Therefore the yields of our Case B models for CVMSs can explain these abundance patterns better than those of PISNe.

4.2.2. Intergalactic Medium

The abundances in the intergalactic medium (IGM) at high redshift also provide important information on the early chemical evolution of the universe. Many researchers have attempted to measure the metallicity of IGM at high redshift (Songaila & Cowie 1996; Songaila 2001; Schaye et al. 2003). Aguirre et al. (2004) observed the abundances of C and Si in IGM at redshift $1.5 \lesssim z \lesssim 4.5$, argued that Si and C have the same origin, and obtained $[\text{C}/\text{Si}] \sim -0.77$. This value is considerably lower than the yields by Population III ordinary massive stars ($M \lesssim 40M_{\odot}$) (see also Heger & Woosley 2002; Chieffi & Limongi 2002; Umeda & Nomoto 2002).

Matteucci & Calura (2005) discussed whether this ratio could be reproduced with their chemical evolution models and obtained $[\text{C}/\text{Si}] = -2.0$ - -1.7 by including the contribution

of Pop III stars over $100M_{\odot}$. This is too small to be compatible with the observed value. Thus they concluded that the contribution of VMSs could not be large. However, they adopted the yields of PISNe ($130 - 300M_{\odot}$) only (Umeda & Nomoto 2002; Heger & Woosley 2002). PISNe enrich much more Si than C.

Although there is a similar feature between PISNe and CVMSs in that $[C/Fe] < 0$, $[Si/Fe] > 0$ and thus $[C/Si] < 0$, $[C/Si]$ from CVMSs is not so extreme as that by PISNe. With our yields of $1000M_{\odot}$ CVMS, $[C/Si] \sim -0.86 - -0.68$ (including both high and low resolution models of $1000M_{\odot}$), which is more than 10 times larger than the results by Matteucci & Calura (2005). Our values are compatible with the observed value (Aguirre et al. 2004), and they show that the contribution of CVMS to the IGM enrichment is significant.

4.2.3. *Extremely Metal-Poor Stars*

Figure 16 compares the yields of our models with extremely metal-poor (EMP) stars in the Galactic halo (the data by Cayrel et al. 2004). The result is that our Case B CVMS models mostly agree with these Galactic halo star data for both α -elements and iron-peak elements. $[Mg/Fe]$ in the EMP stars is oversolar for a wide range of metallicity. $[Cr/Fe]$ and $[Mn/Fe]$ are small while $[Co/Fe]$ and $[Zn/Fe]$ are large. Cr (produced as ^{48}Ti) and Mn (produced as ^{55}Co) are mainly produced in the incomplete silicon burning region, while Co (produced as ^{59}Cu) and Zn (produced as ^{64}Ge) are mainly produced in the complete silicon burning region. We note that the aspherical models for ordinary massive stars with $25M_{\odot}$ and $40M_{\odot}$ in Maeda & Nomoto (2003) are also consistent with EMP star's abundance patterns. Umeda & Nomoto (2003) obtained similar results with spherical models by introducing a mixing and fallback scenario.

It has been reported that $[O/Fe]$ is generally oversolar for EMP stars, which does not agree with our models. However, there are little data for $[O/Fe]$ at $[Fe/H] \lesssim -3$ and the uncertainties involved in the non-local thermal equilibrium (NLTE) effects and 3D effects may be too large to make conclusive statements. Therefore, to answer the question of whether metal-free CVMSs could contribute to the enrichment at $[Fe/H] < -3$, we will need more accurate observational data of $[O/Fe]$.

5. Summary & Discussion

5.1. Summary

We first calculated the evolution of Pop III CVMSs with $M = 500M_{\odot}$ and $1000M_{\odot}$ from the pre-main-sequence through the collapse with spherical symmetry. These CVMSs are thought not to explode if they undergo spherical collapse (Fryer et al. 2001). We assumed that these stars explode in a form of bipolar jets, and explored the required constraints. The results of our nucleosynthesis calculations were used to examine their contribution to the chemical evolution of galaxies. Our major findings are:

- 1 The region which experiences explosive silicon burning to produce iron-peak elements is more than 20% of the total mass, much larger than those of ordinary massive stars such as a $25M_{\odot}$ star. Note that for the metal-free $25M_{\odot}$ star model, this fraction is less than 10% (Umeda & Nomoto 2002). This is because for the $500M_{\odot}$ and $1000M_{\odot}$ models the density and temperature distributions are much flatter than those of $25M_{\odot}$ stars.
- 2 Typical explosion energy is of the order of 10^{54} erg for $1000M_{\odot}$ models for the parameter ranges in this study.
- 3 Black hole masses are $\sim 500M_{\odot}$ for the $1000M_{\odot}$ star models. Note that such a black hole mass is very similar to those of IMBHs, e.g., a claimed $\sim 700M_{\odot}$ black hole in M82. It is quite possible that CVMSs could be the progenitors of IMBHs.
- 4 Nucleosynthesis yields of CVMS have similar patterns of $[\alpha/\text{Fe}]$ to the observed abundance patterns of both ICM and gases of the central region of M82 if the contribution of the jet is small (Case B). Specifically, for Case B small ratios of $[\text{O}/\text{Fe}]$ and $[\text{Ne}/\text{Fe}]$ combined with large $[\text{Mg}/\text{Fe}]$, $[\text{Si}/\text{Fe}]$ and $[\text{S}/\text{Fe}]$ (i.e. large $[(\text{Mg}, \text{Si}, \text{S})/\text{O}]$) are generally more consistent with these observational data than those of hypernovae and PISNe.
- 5 For IGM, $[\text{C}/\text{Si}]$ of our CVMS models is compatible with that of IGM at high redshift ($z = 5$), which is sufficiently higher than those of PISNe.
- 6 For Fe-peak elements, the main feature of the yields of our Case B CVMSs is that $[\text{Cr}/\text{Fe}]$ and $[\text{Mn}/\text{Fe}]$ are small while $[\text{Co}/\text{Fe}]$ and $[\text{Zn}/\text{Fe}]$ are large. This is consistent with the observed ratios in the extremely metal-poor (EMP) stars. The oversolar ratios of some α -elements, such as $[\text{Mg}/\text{Fe}]$ and $[\text{Si}/\text{Fe}]$, are also consistent with EMP stars. Our CVMS models do not agree with the oversolar $[\text{O}/\text{Fe}]$ of EMP stars. However,

more data of $[\text{O}/\text{Fe}]$ in EMP stars will be needed in order to see whether CVMSs can contribute to the early galactic chemical evolution. In this sense $[\text{O}/\text{Fe}]$ would be important to discriminate between different models.

5.2. Discussion

5.2.1. Mass Accretion and Mass Loss

It was pointed out (Omukai & Palla 2003; Tan & McKee 2004) that after a protostar starts shining as a main-sequence star the accretion still continues. In our current study, as a starting point the effect of accretion on mass growth during the presupernova evolution is not included. In our next more realistic models such accretion will be included in the evolutionary calculations also. However, Omukai & Palla (2003) find that when the protostar simulation of very massive stars is carried out properly with time-dependent accretion rates, the rates generally decrease toward the end of the protostar era and after the onset of the main-sequence stellar phase.

Also, it was pointed out (Maeder & Meynet 2004) that mass loss will not be negligible even for zero-metallicity stars when they are rotating, and hence mass loss also will be included in the next step of our models. However, we expect that our major conclusions as summarized above are still valid, at least qualitatively. Somewhat more massive CVMSs, however, may be needed to obtain the same mass black holes if mass loss is significant.

5.2.2. Reionization and Chemical Enrichment

For our CVMSs, the timescale of evolution from the zero-age main sequence to core-collapse is $\sim 2 \times 10^6$ years – only 1/3 - 1/10 as long as for ordinary massive stars (13 - 25 M_{\odot}). So if these CVMSs were formed as the first generation stars they would be the first contributor to reionize and enrich the universe (Omukai & Palla 2003; Tumlinson & Shull 2000; Bromm et al. 2001; Schaerer 2002).

Concerning the existence of VMSs, it was proposed (e.g., see Wasserburg, & Qian 2000; Qian et al. 2002; Qian & Wasserburg 2002) that the prompt inventory involving VMSs produced the elements from C to the Fe group, in order to explain the observed jump in the abundances of heavy r-process elements at $[\text{Fe}/\text{H}] \sim -3$, and also that while VMSs themselves produced no heavy r-elements, these stars dominated chemical evolution earlier at $[\text{Fe}/\text{H}] < -3$. Some others (e.g., Venkatesan & Truran 2003; Tumlinson, Venkatesan, &

Shull 2004) argue that various observational data on reionization, the microwave background, the metal enrichment of the high redshift IGM, etc., indicate that the IMF of the first stars need not necessarily have been biased toward high masses. In what follows, we revisit this issue on the basis of our present models.

In section §3.4 we estimated the ionization efficiency of our CVMSs. It was found that the number of ionizing photons per baryon in the universe, generated in association with the IGM metallicity $Z_{\text{IGM}} \sim 10^{-4}$, is $N_{\text{Lyc}}/N_{\text{b}} \sim 150$, and so CVMSs can contribute significantly to reionization of IGM in the early epoch. Here we emphasize that our current result for CVMS is contributed from the mass range with $\sim 300 - 1000 M_{\odot}$, and hence the PISN (pair instability supernova) range is not included. On the other hand, Venkatesan & Truran (2003) give $N_{\text{Lyc}}/N_{\text{b}} \sim 10$ for $Z_{\text{IGM}} \sim 10^{-4}$ for the mass range $\sim 100 - 1000 M_{\odot}$ which reflects the large contribution of PISNe to metal enrichment. Daigne et al. (2004) also considered reionization and chemical enrichment of IGM simultaneously and reached similar conclusion that VMSs are not necessary. However, in their models CVMSs do not explode. Here we may note that less massive Pop III stars ($\lesssim 100 M_{\odot}$) can also produce the amount of ionizing photons per metal similar to CVMS (Venkatesan & Truran 2003; Tumlinson et al. 2004).

The relation between reionization and metal enrichment of IGM becomes clearer if we solve the equation for $N_{\text{Lyc}}/N_{\text{b}}$ (Eqn. 2 of Venkatesan & Truran 2003) for a given value of Z_{IGM} . For a $1000 M_{\odot}$ star, $Z/Z_{\odot} \sim 10^{-3.4}$ and $10^{-4.4}$ for the required number of ionizing photons per baryon 10 and 1, respectively. This is about one order of magnitude smaller than the case for the mass range $100 - 1000 M_{\odot}$ (mainly contributed by PISNe). The difference between CVMSs and PISNe is larger if we consider the enrichment of iron. The $260 M_{\odot}$ PISN of Heger & Woosley (2002) gives $Z_{\text{Fe}}/Z_{\text{Fe},\odot} \sim 10^{-2} - 10^{-3}$, while our $500 M_{\odot}$ and $1000 M_{\odot}$ star gives $\sim 10^{-3.2} - 10^{-4.2}$.

A main critique against the existence of PISNe comes from the fact that we do not see the abundance patterns of PISNe in EMP stars (Umeda & Nomoto 2002; Tumlinson et al. 2004). The EMP abundances are indeed suggested to be accounted for by hypernovae or faint supernovae of less massive stars of $\lesssim 100 M_{\odot}$ (Umeda & Nomoto 2003). However, the apparent lack of evidence of VMSs by no means contradicts the existence of CVMSs at earlier epochs, if the majority of first stars in the earlier epoch has masses $\gtrsim 300 M_{\odot}$. First, PISNe from stars of $\lesssim 300 M_{\odot}$ will be just a minor fraction in such a case, explaining the lack of the signature of PISNe. Second, Z/Z_{\odot} expected from our CVMSs is smaller than PISNe. Namely, the metal enrichment by CVMSs might be finished before ordinary core-collapse SNe become dominant. Note that the abundance, especially of oxygen, in EMP stars and IGM is different. Here we have shown that the yields of our CVMSs can reproduce the abundance of IGM (Section 4). Therefore, it would be worthwhile studying a scenario

where CVMSs are first formed in pregalactic mini halos, and then subsequently ordinary core-collapse SNe took place in the galactic halo.

We mentioned that the early universe would have been contaminated too much if there were many PISNe. This conclusion is not affected when the calculation of PISNe considers the effect of rotation and asymmetric explosion (see Stringfellow & Woosley 1988). In PISNe with rotation, all matter is ejected with nothing left as in non-rotating models, and the total amount of matter ejected is almost independent of the geometry of the explosion, whether spherical or not. The explosive nucleosynthesis itself and hence the resulting exact composition of the ejected matter change with rotation and under the consequent asymmetric environment, but that does not change our conclusion that too many of PISNe result in the overabundance of heavy elements in the early universe which contradicts with the observation.

5.2.3. *Initial Mass Function*

Tumlinson et al. (2004) raised two problems associated with top heavy IMF of the first stars. (a) If stars are all $M \gtrsim 300M_\odot$, no metals are released from Pop III stars to trigger the transition from the first stars to present IMF star formation, and (b) no mechanism has been proposed for forming stars more massive than $\sim 300M_\odot$ without forming PISNs.

Here we discuss how our CVMS models could resolve these apparent problems. Concerning (a), our present CVMS models do eject metals (though less than PISNe), leading to metal enrichment of IGM. In this connection, note that the existing literature concerning the effects of VMSs (in Pop III IMF) on reionization, etc., includes only contribution by PISNs but not those heavier because they assumed that heavier stars do not explode, and hence make no contribution. However, we emphasize the importance of the explosion of these heavier stars ($\gtrsim 500M_\odot$).

Concerning (b), collisions and merging of ordinary massive stars in very dense clusters are expected to lead to the formation of more massive stars (Ebisuzaki et al. 2001; Portegies Zwart et al. 1999, 2004a, 2004b) which can easily lead to CVMSs ($\gtrsim 300M_\odot$) without or with only minor fraction of stars responsible for PISNe ($\lesssim 300M_\odot$), and hence the problem in question can disappear. Specifically, in this scenario PISN stars will have no time to explode before merging into heavier stars when the timescale of the PISN star evolution is longer than merging timescale. Also, even in the case of single star formation (no merging) there is yet no reason to exclude a possibility of the first star IMF with the minimum mass of $\sim 300M_\odot$.

As to the question of how CVMSs are formed, the first generation stars are generally thought to have formed in low-mass halos with the virial temperature $T_{\text{vir}} < 10^4$ K. Then the upper limit to the mass of first stars may be $\sim 300M_{\odot}$ (e.g., Bromm & Loeb 2004). However, Oh & Haiman (2002) investigated halos with higher mass, with $T_{\text{vir}} > 10^4$ K. The evolution of these high mass halos, e.g., of $\sim 10^9M_{\odot}$, is found to be quite different from the low mass case, and the degree of fragmentation of the gas is still highly uncertain. Therefore, it appears that whether more massive stars can be directly formed is still an open question. However, regardless of the feasibility of direct formation, it has been emphasized by, e.g., Ebisuzaki et al. (2001), and Portegies Zwart et al. (1999, 2004a, 2004b), that CVMSs will be formed easily by merging of less massive stars in very dense star clusters, and hence there appears to be essentially no problem for CVMS formation.

5.2.4. Black Hole Mass

As to the existence of IMBHs, currently extensive effort is under way to try to detect them in nearby galaxies (see, e.g., Barth et al. 2005 for recent review). Already several of these objects have been identified, mostly in dwarf elliptical galaxies, but some in spiral galaxies, e.g., M33, IC 342, Pox 52, NGC 4395 and several galaxies in the Sloan Digital Sky Survey (SDSS) sample. For example, the black hole mass obtained for M33 is less than $\sim 3000M_{\odot}$ but larger than the mass of a stellar mass black hole. The black hole mass obtained for NGC 4395 is $\sim 10^4 - 10^5M_{\odot}$, but its spectra are unlike NLSI (narrow line Seyfert I) - a class of AGN which tends to have small mass. We expect more of these IMBH candidates, with better mass measurement, to be identified in the very near future.

As an example of possibly more recently formed IMBHs, Matsumoto et al. (2001) reported the possible discovery of a $\gtrsim 700M_{\odot}$ black hole in M82 as an ULX (ultra-luminous X-ray source). Since an ULX was first detected in 1989 by the *Einstein* Observatory (Fabiano 1989), many of these objects have been discovered. Possible scenarios for formation of IMBHs associated with ULXs are speculated in a recent article by Krolik (2004). Colbert & Mushotzky (1999) first suggested that these luminous objects are indeed IMBHs, because their luminosity is super Eddington for stellar mass black holes if spherical accretion is adopted. That may not be necessary if beaming, etc., is assumed. However, ULXs may be heterogeneous, and at least some of these objects may well prove to be IMBHs. The prospect is bright because various observations in multifrequency bands can distinguish between different interpretations.

This work has been supported in part by the Grant-in-Aid for Scientific Research

(15204010, 16540229, 17030005, 17033002) and the 21st Century COE Program (QUEST) from the JSPS and MEXT of Japan.

We thank the referee for useful comments.

REFERENCES

- Abel, T., Bryan, G.L., & Norman, M.L. 2000, *ApJ*, 540, 39
- Aguirre, A., Schaye, J., Kim, T.-S., Theuns, T., Rauch, M., & Sargent, W. L. W. 2003, *ApJ*, 602, 38
- Arnett, W. D. 1996, *Supernovae and Nucleosynthesis* (Princeton:Princeton University Press)
- Baraffe, I., Heger, A., & Woosley, S. E. 2001, *ApJ*, 550, 890
- Barth, A. J., Green, J. E., & Ho, L. C. 2005, in *Growing Black Holes*, eds. A. Merloni, S. Nayakshin, & R. A. Sunyaev (Springer), 154
- Baumgartner, W. H., Loewenstein, M., Horner, D. J., & Mushotzky, R.F. 2005, *ApJ*, 620, 680
- Bender, R. 2005, in *Growing Black Holes*, eds. A. Merloni, S. Nayakshin, & R. A. Sunyaev (Springer), 147
- Bond, J. R., Arnett, W. D., & Carr, B. J. 1984, *ApJ*, 280, 825
- Bromm, V., Kudritzki, R. P., & Loeb, A. 2001, *ApJ*, 552, 464
- Bromm, V., Coppi, P.S., & Larson, R.B. 2002, *ApJ*, 564, 23
- Bromm, V., & Loeb, A. 2003, *ApJ*, 596, 34
- Bromm, V., & Loeb, A. 2004, *NewA*, 9, 353
- Cayrel, R., et al. 2004, *A& A*, 416, 1117
- Chieffi, A., & Lomongi, M. 2002, *ApJ*, 577, 281
- Colbert, E.J., & Mushotzky, R. 1999, *Ap.J.* 519, 89
- Daigne, F., Olive, K. A., Vangioni-Flam, E., Silk, J., & Audouze, J. 2004, *ApJ*, 617, 693
- Ebisuzaki, T., et al. 2001, *ApJ*, 562, L19

- Fabbiano, G. 1989, *ARA&A*, 27, 87
- Fryer, C. L., Woosley, S. E., & Heger, A. 2001, *ApJ*, 550, 372
- Glatzel, W., Fricke, K. J., & El Eid, M. F. 1985, *A&A*, 149, 413
- Gnedin, N. Y., & Ostriker, J.P. 1997, *ApJ*, 486, 581
- Hachisu, I., Matsuda, T., Nomoto, K., & Shigeyama, T. 1992, *ApJ*, 390, 230
- Hachisu, I., Matsuda, T., Nomoto, K., & Shigeyama, T. 1994, *A&A*, 104, 341
- Heger, A., Baraffe, I., Fryer, C.L., Woosley, S.E. 2001, *Nuc. Phys. A.*, 688, 197
- Heger, A., & Woosley, S. E. 2002, *ApJ*, 567, 532
- Hix, W. R. & Thielemann, F.-K. 1996, *ApJ*, 460, 869
- Ibrahim, A., Boury, A., & Noels, A. 1981, *A&A*, 103, 390
- Khokhlov, A. M., Höflich, P. A., Oran, E. S., Wheeler, J. C., Wang, L., & Chtchelkanova, A. Y. 1999, *ApJ*, 524, L107
- Kogut, A., et al. 2003, *ApJS*, 148, 161
- Kormendy, J., & Richstone, D. 1995, *ARA&A*, 33, 581
- Krolik, J. H. 2004, *ApJ*, 615, 383
- Kudritzki, R.-P. 2000, in *The First Stars*. eds. A. Weiss, T. G. Abel, & V. Hill (Berlin: Springer), 127
- Loewenstein, M. 2001, *ApJ*, 557, 573
- MacFadyen, A. I., Woosley, W. E., & Heger, A. 2001, *ApJ*, 550, 410
- MacFadyen, A. I. 2003, in *From Twilight to Highlight: The Physics of Supernovae*, eds. W. Hillebrandt & B. Leibundgut (Berlin: Springer), 97 (astro-ph/0301425)
- MacFadyen, A. I. & Woosley, S. E. 1999, *ApJ*, 524, 262
- Maeda, K., Nakamura, T., Nomoto, K., Mazzali, P. A., Patat, F., & Hachisu, I. 2002, *ApJ*, 565, 405
- Maeda, K., & Nomoto, K. 2003, *ApJ*, 598, 1163

- Maeda, K. 2004, Ph.D.thesis, the University of Tokyo
- Maeda, K., Nomoto, K., Mazzali, P. A., & Deng, J. 2006, ApJ, 640, in press (astro-ph/0508373)
- Maeder, A., & Meynet, G. 2004, A&A, 422, 225
- Marchant, A. B., & Shapiro, S. L. 1980, ApJ, 239, 685
- Matsumoto, H., Tsuru, T. G., Koyama, K., Awaki, K., Canizares, C. R., Kawai, N., Matsushita, S., & Kawabe, R. 2001, ApJ, 547, L25
- Matteucci, F., & Calura, F. 2005, MNRAS, 360, 447
- Nagataki, S. 2000, ApJS, 127, 141
- Nakamura, F. & Umemura, M. 1999, ApJ, 515, 239
- Nakamura, T., Umeda, H., Iwamoto, K., Nomoto, K., Hashimoto, M., Hix, W. R., & Thielemann, F.-K. 2001, ApJ, 555, 880
- Narayan, R., Piran, T., & Kumer, P. 2001, ApJ, 557, 949
- Nomoto, K. & Hashimoto, M. 1988, Phys. Rep., 163, 13
- Nomoto, K., et al. 2003, in IAU Symp 212, A Massive Star Odyssey, from Main Sequence to Supernova, eds. V. D. Hucht, et al. (ASP), 395 (astro-ph/0209064)
- Oh, S. P., & Haiman, Z. 2002, ApJ, 569, 558
- Omukai, K. & Palla, F. 2003, ApJ, 589, 677
- Origlia, L., Ranalli, P., Comastri, A., & Maiolino, R. 2004, ApJ, 606, 862
- Peterson, J. R., Kahn, S. M., Paerels, F. B. S., Kaastra, J. S., Tamura, T., Bleeker, J. A. M., Ferrigno, C., & Jernigan, J. G. 2003, ApJ, 590, 207
- Portegies Zwart, S. F., Makino, J., McMillan, S. L. W., & Hut, P. 1999, A&A, 348, 117
- Portegies Zwart, S. F., Baumgardt, H., Hut, P., Makino, J., & McMillan, S.L.W. 2004a, Nature, 428, 724
- Portegies Zwart, S.F. 2004b, in Joint Evolution of Black Holes and Galaxies, eds. M. Colpi, V. Gorini, F. Haardt & U. Moschella (Bristol and Philadelphia: IOP Publishing), in press (astro-ph/0406550)

- Pruet, J., Surman, R., & McLaughlin, G.C. 2004, *ApJ*, 602, L101
- Qian, Y.-Z., Sargent, W.L.W., & Wasserburg, G.J. 2002, *ApJ*, 588, 1099
- Qian, Y.-Z., & Wasserburg, G.J. 2002, *ApJ*, 567, 515
- Rakavy, G., Shaviv, G., & Zinamon, Z. 1967, *ApJ*, 150, 131
- Ranalli, P., Origlia, A., Comastri, A., Maiolino, R., & Makishima, K. 2005, in *The X-ray Universe 2005*, held in San Lorenzo de el Escorial, September 2005 (astro-ph/0511021)
- Rees, M. J. 2002, in *Lighthouses of the universe: Most Luminous Celestial Objects and Their Use for Cosmology*, eds. M. Gilfanov, R. Sunyaev, & E. Churazov (Springer), 345
- Rees, M. J. 2003, in *The Future of Theoretical Physics and Cosmology*, eds. G. W. Gibbons, E. P. S. Shellard, & S. J. Rankin, 217
- Schaerer, D. 2002, *A&AS*, 382, 28
- Schaye, J., Aguirre, A., Kim, T.-S., Theuns, T., Rauch, M., & Sargent, W. L. W. 2003, *ApJ*, 596, 768
- Shibata, M. & Shapiro, S. L. 2002, *ApJ*, 572, L39
- Somerville, R. S., Bullock, J. S., & Livio, M. 2003, *ApJ*, 593, 616
- Songaila, A. 2001, *ApJ*, 561, 153
- Songaila, A., & Cowie, L. L. 1996, *AJ*, 112, 335
- Stringfellow, G. S., & Woosley, S. E. 1988, in *The Origin and Distribution of the Elements*, ed. G. J. Mathews (Singapore: World Scientific Press), 467
- Tan, J. C., & McKee, C. F. 2004, *ApJ*, 603, 383
- Thielemann, F.-K., Nomoto, K., & Hashimoto, M. 1996, *ApJ*, 460, 408
- Tsuru, T. G., Awaki, H., Koyama, K., & Ptak, A. 1997, *PASJ*, 49, 619
- Tumlinson, J. & Shull, J. H. 2000, *ApJ*, 528, L65
- Tumlinson, J., Venkatesen, A., & Shull, J. M. 2004, *ApJ*, 612, 602
- Umeda, H., Nomoto, K., & Nakamura, T. 1999, in *The First Stars*, eds. A. Weiss et al. (Berlin: Springer), 150 (astro-ph/9912248)

- Umeda, H., Nomoto, K., Tsuru, T. G., & Matsumoto, H. 2002, *ApJ*, 578, 855
- Umeda, H. & Nomoto, K. 2002, *ApJ*, 565, 385
- Umeda, H. & Nomoto, K. 2003, *Nature*, 422, 871
- Venkatesan, A., Tumlinson, J., & Shull, J. M. 2003, *ApJ*, 584, 621
- Venkatesan, A., & Truran, J.W. 2003, *ApJ*, 594, L1
- Wasserburg, G.J., & Qian, Y.-Z. 2000, *ApJ*, 529, L21
- Woosley, S. E. 1986, in *Nucleosynthesis and Chemical Evolution* eds. B. Hauck, A. Maeder, & G. Meynet (Switzerland:Geneva Obs.), 1
- Yoshida, N., Bromm, B., & Hernquist, L. 2000, *ApJ*, 605, 579

Table 1. The higher resolution models.

Models	progenitor(M_\odot)	$M_{\text{BH0}}(M_\odot)$	$R_0(\text{km})$	$\theta_{\text{jet}}^\circ$	ϵ	μ	F_{thermal}	v_{jet}/c
A-1	1000	100	1.5×10^4	15	0.01	0.1	0.01	0.45
A-2	1000	100	1.5×10^4	30	0.01	0.1	0.01	0.45
B-1	1000	100	1.5×10^4	15	0.01	0.005	0.95	0.45
B-2	1000	100	1.5×10^4	15	0.005	0.0025	0.95	0.45
B-3	500	50	1.1×10^4	15	0.01	0.005	0.95	0.45

Note. — initial black hole mass M_{BH0} , the radius at the inner boundary of the simulations R_0 , jet injected angle θ_{jet} , energy tranformation efficiency ϵ , the mass fraction in which accreted matter is ejected as jet μ , and the jet velocity normalized by the speed of light v_{jet} .

Table 2. The lower resolution models.

Models	progenitor(M_\odot)	$M_{\text{BH0}}(M_\odot)$	$R_0(\text{km})$	$\theta_{\text{jet}}^\circ$	ϵ	μ	F_{thermal}	v_{jet}/c
A-3	1000	100	1.5×10^4	15	0.005	0.05	0.01	0.45
A-4	1000	100	1.5×10^4	15	0.002	0.02	0.01	0.45
A-5	1000	50	8.4×10^3	15	0.005	0.05	0.01	0.45
A-6	1000	200	2.7×10^4	15	0.01	0.1	0.01	0.45
A-7	500	50	8.4×10^3	15	0.01	0.1	0.01	0.45
B-2	1000	100	1.5×10^4	15	0.005	0.0025	0.95	0.45
B-4	1000	100	1.5×10^4	15	0.01	0.02	0.9	0.32
B-5	1000	100	1.5×10^4	15	0.005	0.01	0.9	0.32

Table 3. Characteristics of explosion models in Table 1.

Models	E (erg)	$M_{\text{BH}}(M_{\odot})$	$M_{\text{e0}}(M_{\odot})$	$M_{\text{jet}}(M_{\odot})$	$M_{\text{e}}(M_{\odot})$
A-1	6.7×10^{54}	5.0×10^2	4.6×10^2	44	5.0×10^2
A-2	2.2×10^{54}	4.4×10^2	5.2×10^2	38	5.6×10^2
B-1	4.9×10^{54}	4.6×10^2	5.4×10^2	1.8	5.4×10^2
B-2	1.6×10^{54}	4.8×10^2	5.2×10^2	0.94	5.2×10^2
B-3	2.9×10^{54}	2.3×10^2	2.7×10^2	0.90	2.7×10^2

Note. — Explosion energy E , final black hole mass M_{BH} , ejected mass excluding jet material M_{e0} , mass of jet M_{jet} , and total ejected mass M_{e} .

Table 4. Same as Table 3, but for the models in Table 2.

Models	E (erg)	$M_{\text{BH}}(M_{\odot})$	$M_{\text{e0}}(M_{\odot})$	$M_{\text{jet}}(M_{\odot})$	$M_{\text{e}}(M_{\odot})$
A-3	4.0×10^{54}	5.3×10^2	4.5×10^2	23	4.7×10^2
A-4	5.2×10^{53}	5.6×10^2	4.3×10^2	9.5	4.4×10^2
A-5	3.0×10^{54}	5.1×10^2	4.5×10^2	45	4.9×10^2
A-6	8.2×10^{54}	5.1×10^2	4.6×10^2	34	4.9×10^2
A-7	6.1×10^{54}	2.4×10^2	2.4×10^2	21	2.6×10^2
B-2	1.9×10^{54}	4.8×10^2	5.2×10^2	0.95	5.2×10^2
B-4	6.4×10^{54}	4.6×10^2	5.3×10^2	7.4	5.4×10^2
B-5	1.8×10^{54}	4.7×10^2	5.3×10^2	3.7	5.3×10^2

Table 5. The models in which explosion does not occur.

Models	progenitor(M_{\odot})	$M_{\text{BH0}}(M_{\odot})$	$\theta_{\text{jet}}^{\circ}$	ϵ	μ	F_{thermal}	v_{jet}/c
F-1	1000	100	15	0.001	0.01	0.01	0.45
F-2	1000	100	30	0.005	0.05	0.01	0.45
F-3	1000	100	45	0.01	0.1	0.01	0.45
F-4	1000	100	15	0.003	0.0015	0.95	0.45

Table 6. Ejected mass of ^{56}Ni , ^{16}O , ^{28}Si , excluding jet material for higher resolution models.

Models	$M(^{56}\text{Ni}) (M_{\odot})$	$M(^{16}\text{O}) (M_{\odot})$	$M(^{28}\text{Si}) (M_{\odot})$
A-1	1.5	4.5	0.69
A-2	12	18	4.3
B-1	9.3	23	6.1
B-2	4.7	24	4.0
B-3	8.9	10	4.8

Table 7. Same as Table 6, but for lower resolution models.

Models	$M(^{56}\text{Ni}) (M_{\odot})$	$M(^{16}\text{O}) (M_{\odot})$	$M(^{28}\text{Si}) (M_{\odot})$
A-3	0.4	2.1	0.24
A-4	0.12	1.2	0.080
A-5	0.36	2.4	0.23
A-6	1.4	5.1	0.77
A-7	1.1	1.8	0.41
B-2	4.4	22	3.8
B-4	7.0	24	5.3
B-5	5.8	25	4.6

Table 8. Nucleosynthesis products (M_\odot) of models A-1, B-1, B-2, and B-3.

Models	A-1	B-1	B-2	B-3		A-1	B-1	B-2	B-3
n	1.68E-13	6.94E-12	5.19E-13	5.65E-14	⁵⁰ Cr	1.04E-03	1.75E-04	9.71E-05	1.29E-04
p	1.90E+02	1.94E+02	1.94E+02	9.59E+01	⁵¹ Cr	1.75E-05	8.55E-07	7.88E-07	6.45E-07
d	2.78E-15	3.65E-15	2.84E-15	4.00E-15	⁵² Cr	3.81E-05	1.61E-06	8.16E-07	9.77E-07
³ He	2.12E-04	2.12E-04	2.12E-04	2.02E-05	⁵³ Cr	6.53E-09	4.55E-10	2.15E-10	2.28E-10
⁴ He	2.72E+02	2.85E+02	2.83E+02	1.43E+02	⁵⁴ Cr	4.17E-10	1.30E-10	5.06E-11	8.69E-11
⁶ Li	1.09E-18	9.64E-18	1.20E-17	6.99E-18	⁵⁵ Cr	7.20E-12	1.41E-10	4.98E-11	5.59E-11
⁷ Li	2.77E-14	1.36E-13	1.52E-13	3.47E-14	⁴⁸ Mn	6.84E-05	2.99E-06	1.37E-06	1.40E-06
⁷ Be	3.77E-09	3.86E-09	3.89E-09	1.86E-09	⁴⁹ Mn	3.54E-04	1.12E-04	2.88E-05	6.88E-05
⁹ Be	6.40E-21	3.83E-19	3.10E-20	8.71E-21	⁵⁰ Mn	2.30E-04	6.94E-05	2.08E-05	3.61E-05
⁸ B	2.93E-14	3.05E-14	3.05E-14	4.54E-13	⁵¹ Mn	1.16E-03	2.68E-04	9.65E-05	1.56E-04
¹⁰ B	7.04E-15	8.02E-14	9.11E-14	2.96E-14	⁵² Mn	1.09E-04	9.84E-06	7.71E-06	9.95E-06
¹¹ B	1.08E-15	1.22E-14	1.20E-14	5.68E-15	⁵³ Mn	1.66E-04	2.00E-05	1.37E-05	2.87E-05
¹¹ C	1.74E-12	1.05E-11	4.28E-12	3.14E-12	⁵⁴ Mn	3.20E-07	1.38E-08	6.94E-09	7.63E-09
¹² C	8.11E-01	3.56E+00	3.68E+00	7.61E-01	⁵⁵ Mn	1.73E-08	9.05E-10	4.36E-10	5.97E-10
¹³ C	6.07E-09	2.23E-08	2.30E-08	4.58E-08	⁵⁶ Mn	8.12E-12	1.03E-10	4.28E-11	8.74E-11
¹³ N	1.16E-10	3.20E-10	6.14E-10	2.31E-08	⁵⁷ Mn	7.48E-12	1.08E-10	4.22E-11	7.60E-11
¹⁴ N	1.16E-05	3.49E-05	2.77E-05	7.15E-06	⁵⁰ Fe	2.01E-04	1.09E-05	3.63E-06	4.36E-06
¹⁵ N	3.13E-09	1.30E-07	3.93E-08	1.40E-07	⁵¹ Fe	4.36E-04	5.11E-05	9.14E-06	1.84E-05
¹⁴ O	2.54E-05	9.14E-04	1.86E-04	1.41E-04	⁵² Fe	4.31E-02	9.34E-02	5.22E-02	8.61E-02
¹⁵ O	2.18E-06	7.72E-06	4.25E-06	5.12E-06	⁵³ Fe	1.36E-03	3.34E-03	2.00E-03	3.61E-03
¹⁶ O	4.55E+00	2.31E+01	2.37E+01	1.03E+01	⁵⁴ Fe	2.26E-03	5.19E-03	4.99E-03	1.11E-02
¹⁷ O	1.74E-08	1.29E-07	5.67E-08	3.57E-08	⁵⁵ Fe	3.96E-05	3.52E-06	2.16E-06	1.06E-05
¹⁸ O	2.50E-07	5.92E-07	9.19E-07	6.93E-11	⁵⁶ Fe	5.40E-05	2.73E-06	1.33E-06	6.56E-06
¹⁷ F	1.24E-08	2.86E-09	1.58E-09	7.01E-10	⁵⁷ Fe	6.49E-08	2.94E-09	1.45E-09	1.63E-09
¹⁸ F	8.20E-08	8.77E-06	1.25E-06	7.24E-07	⁵⁸ Fe	6.00E-09	4.07E-10	1.87E-10	2.09E-10
¹⁹ F	6.80E-11	5.56E-08	1.37E-09	1.43E-08	⁵⁹ Fe	6.49E-12	1.16E-10	5.11E-11	6.46E-11
¹⁸ Ne	6.92E-06	3.10E-07	1.48E-07	4.68E-07	⁶⁰ Fe	7.62E-12	1.31E-10	4.37E-11	7.54E-11
¹⁹ Ne	2.91E-07	1.07E-06	2.77E-08	5.09E-07	⁶¹ Fe	3.56E-12	1.20E-10	2.07E-11	7.08E-11
²⁰ Ne	7.83E-01	5.18E+00	4.82E+00	1.58E+00	⁵¹ Co	2.89E-10	1.19E-11	5.95E-12	5.71E-12
²¹ Ne	1.23E-05	2.56E-05	4.48E-05	2.35E-05	⁵² Co	1.22E-05	4.82E-07	2.27E-07	2.35E-07
²² Ne	1.34E-05	2.27E-05	4.64E-05	1.50E-06	⁵³ Co	1.56E-04	1.39E-05	4.15E-06	6.23E-06
²¹ Na	4.98E-07	2.84E-06	6.22E-07	1.44E-06	⁵⁴ Co	3.07E-04	6.25E-05	1.14E-05	3.25E-05
²² Na	1.64E-06	1.13E-05	1.53E-05	3.55E-05	⁵⁵ Co	1.37E-03	3.30E-03	1.79E-03	4.02E-03
²³ Na	4.18E-05	3.46E-04	4.14E-04	5.56E-04	⁵⁶ Co	1.72E-04	1.89E-05	1.32E-05	1.99E-05
²² Mg	2.37E-04	1.58E-05	6.22E-06	1.26E-05	⁵⁷ Co	5.33E-04	2.71E-05	1.60E-05	1.43E-05
²³ Mg	2.14E-04	7.84E-04	9.12E-04	1.04E-03	⁵⁸ Co	7.77E-06	3.29E-07	1.66E-07	1.60E-07
²⁴ Mg	7.05E-01	4.55E+00	4.14E+00	1.43E+00	⁵⁹ Co	3.23E-05	1.37E-06	6.89E-07	6.58E-07
²⁵ Mg	1.47E-04	6.76E-04	7.04E-04	2.88E-04	⁶⁰ Co	4.68E-09	4.20E-10	1.80E-10	2.39E-10
²⁶ Mg	3.65E-05	1.70E-04	1.50E-04	4.11E-05	⁶¹ Co	1.82E-11	2.24E-10	8.42E-11	1.02E-10
²⁷ Mg	1.54E-11	9.35E-10	1.85E-10	3.38E-11	⁶² Co	6.29E-12	1.32E-10	5.11E-11	8.78E-11
²⁵ Al	2.97E-05	1.10E-04	1.25E-05	2.79E-04	⁵⁴ Ni	5.26E-05	1.42E-06	5.54E-07	6.72E-07
²⁶ Al	3.88E-06	1.72E-05	1.42E-05	2.54E-05	⁵⁵ Ni	3.16E-04	1.57E-05	4.70E-06	5.77E-06
²⁷ Al	5.97E-04	7.06E-03	4.95E-03	5.78E-03	⁵⁶ Ni	2.04E+01	1.01E+01	5.07E+00	9.32E+00
²⁸ Al	1.98E-08	5.58E-07	1.88E-07	9.17E-08	⁵⁷ Ni	3.80E-01	1.68E-01	8.32E-02	1.30E-01
²⁹ Al	1.42E-12	7.85E-11	1.31E-11	1.24E-11	⁵⁸ Ni	7.66E+00	3.83E-01	1.93E-01	2.03E-01

Table 8—Continued

Models	A-1	B-1	B-2	B-3		A-1	B-1	B-2	B-3
²⁶ Si	5.63E-04	7.80E-05	2.16E-05	5.95E-05	⁵⁹ Ni	1.47E-01	6.79E-03	3.76E-03	3.47E-03
²⁷ Si	2.62E-04	1.21E-03	1.06E-03	1.14E-03	⁶⁰ Ni	2.31E+00	9.74E-02	5.21E-02	4.69E-02
²⁸ Si	6.92E-01	6.19E+00	4.04E+00	4.81E+00	⁶¹ Ni	2.29E-03	9.65E-05	4.97E-05	4.65E-05
²⁹ Si	3.07E-04	2.26E-03	1.94E-03	3.03E-03	⁶² Ni	2.13E-04	9.00E-06	4.64E-06	4.33E-06
³⁰ Si	1.66E-05	2.38E-04	7.63E-05	5.81E-04	⁶³ Ni	3.05E-08	1.40E-09	6.71E-10	6.68E-10
³¹ Si	4.78E-11	8.74E-09	6.55E-10	3.94E-09	⁶⁴ Ni	6.81E-10	2.02E-10	9.08E-11	1.11E-10
³² Si	5.46E-13	1.14E-11	5.42E-12	3.31E-12	⁶⁵ Ni	6.02E-12	1.32E-10	4.23E-11	7.07E-11
²⁷ P	1.93E-06	8.17E-08	4.11E-08	3.99E-08	⁶⁶ Ni	7.20E-12	2.09E-10	5.35E-11	8.03E-11
²⁸ P	7.79E-05	8.57E-06	2.43E-06	3.40E-06	⁵⁶ Cu	1.23E-09	5.07E-11	2.53E-11	2.45E-11
²⁹ P	1.04E-04	4.08E-04	6.05E-05	1.35E-03	⁵⁷ Cu	1.29E-03	5.67E-05	2.78E-05	2.87E-05
³⁰ P	1.26E-04	3.25E-04	1.75E-04	2.79E-04	⁵⁸ Cu	3.60E-02	4.92E-02	1.41E-02	4.46E-02
³¹ P	8.43E-05	4.22E-04	2.66E-04	7.31E-04	⁵⁹ Cu	4.34E-02	3.67E-02	1.15E-02	3.46E-02
³² P	1.37E-09	5.33E-09	3.76E-09	1.15E-08	⁶⁰ Cu	6.17E-03	3.54E-03	2.70E-03	1.71E-03
³³ P	4.73E-10	1.16E-09	1.25E-09	4.37E-09	⁶¹ Cu	6.53E-02	2.80E-03	1.55E-03	1.35E-03
³⁴ P	1.76E-12	2.02E-11	1.41E-11	2.85E-12	⁶² Cu	2.45E-03	1.04E-04	5.26E-05	5.00E-05
³⁰ S	1.05E-03	1.58E-04	3.32E-05	7.83E-05	⁶³ Cu	1.81E-03	7.66E-05	4.00E-05	3.69E-05
³¹ S	2.60E-04	2.94E-04	9.71E-05	1.88E-04	⁶⁴ Cu	1.85E-06	7.84E-08	3.96E-08	3.78E-08
³² S	3.55E-01	3.17E+00	2.00E+00	2.68E+00	⁶⁵ Cu	7.68E-07	3.26E-08	1.64E-08	1.57E-08
³³ S	1.71E-04	1.11E-03	8.41E-04	1.31E-03	⁶⁶ Cu	1.23E-10	1.65E-10	7.10E-11	8.85E-11
³⁴ S	1.45E-04	3.39E-05	3.47E-05	3.59E-04	⁶⁷ Cu	1.21E-11	2.06E-10	6.61E-11	7.34E-11
³⁵ S	3.83E-10	3.96E-10	4.72E-10	1.77E-09	⁶⁸ Cu	9.76E-12	1.65E-10	5.32E-11	6.91E-11
³⁶ S	1.45E-09	3.52E-10	3.41E-10	2.03E-10	⁵⁹ Zn	1.07E-03	3.81E-04	6.15E-05	6.95E-04
³⁷ S	1.87E-12	2.00E-11	1.48E-11	3.27E-12	⁶⁰ Zn	6.55E-01	3.70E-01	1.29E-01	2.08E-01
³² Cl	4.80E-04	2.21E-05	1.02E-05	1.04E-05	⁶¹ Zn	1.35E-02	2.74E-03	1.51E-03	1.78E-03
³³ Cl	9.07E-05	6.11E-05	9.32E-06	7.32E-05	⁶² Zn	7.68E-01	3.62E-02	1.80E-02	1.93E-02
³⁴ Cl	2.31E-04	7.34E-05	1.68E-05	3.23E-05	⁶³ Zn	2.37E-02	1.06E-03	6.10E-04	5.23E-04
³⁵ Cl	3.10E-04	1.45E-04	5.12E-05	2.93E-04	⁶⁴ Zn	1.06E+00	4.49E-02	2.30E-02	2.16E-02
³⁶ Cl	2.45E-07	3.80E-08	2.64E-08	7.18E-08	⁶⁵ Zn	2.37E-03	1.00E-04	5.13E-05	4.82E-05
³⁷ Cl	1.46E-07	1.60E-08	1.35E-08	3.73E-08	⁶⁶ Zn	2.14E-03	9.02E-05	4.55E-05	4.34E-05
³⁸ Cl	3.17E-12	3.17E-11	2.95E-11	8.79E-12	⁶⁷ Zn	6.02E-07	2.57E-08	1.30E-08	1.24E-08
³⁴ Ar	1.84E-03	1.69E-04	4.99E-05	7.78E-05	⁶⁸ Zn	1.09E-08	6.34E-10	3.16E-10	3.11E-10
³⁵ Ar	8.13E-04	2.26E-04	5.11E-05	9.33E-05	⁶⁹ Zn	9.27E-12	2.04E-10	6.15E-11	7.40E-11
³⁶ Ar	6.96E-02	5.88E-01	3.65E-01	4.97E-01	⁷⁰ Zn	1.00E-11	2.42E-10	6.58E-11	8.77E-11
³⁷ Ar	5.31E-05	1.68E-04	1.16E-04	1.79E-04	⁷¹ Zn	6.19E-12	1.08E-10	4.16E-11	5.50E-11
³⁸ Ar	3.94E-04	4.02E-05	3.34E-05	3.25E-04	⁶¹ Ga	8.83E-05	3.80E-06	1.89E-06	1.84E-06
³⁹ Ar	7.03E-08	3.00E-09	1.53E-09	1.54E-09	⁶² Ga	4.83E-05	5.15E-06	1.67E-06	4.16E-06
⁴⁰ Ar	8.68E-08	3.75E-09	1.89E-09	1.79E-09	⁶³ Ga	1.37E-03	1.39E-03	4.86E-04	9.56E-04
⁴¹ Ar	2.41E-12	3.70E-11	2.57E-11	2.06E-11	⁶⁴ Ga	9.88E-04	4.41E-04	3.13E-04	2.06E-04
⁴² Ar	2.80E-12	4.55E-11	2.62E-11	1.35E-11	⁶⁵ Ga	7.21E-04	3.52E-05	2.43E-05	1.63E-05
⁴³ Ar	4.53E-12	5.33E-11	3.00E-11	1.73E-11	⁶⁶ Ga	8.58E-05	3.66E-06	2.18E-06	1.77E-06
³⁶ K	6.58E-04	3.03E-05	1.39E-05	1.39E-05	⁶⁷ Ga	5.36E-04	2.26E-05	1.15E-05	1.09E-05
³⁷ K	1.11E-04	6.81E-05	1.65E-05	2.06E-05	⁶⁸ Ga	1.44E-06	6.12E-08	3.08E-08	2.95E-08
³⁸ K	7.55E-05	3.07E-05	1.31E-05	9.38E-06	⁶⁹ Ga	1.02E-06	4.32E-08	2.18E-08	2.08E-08
³⁹ K	6.15E-04	6.88E-05	3.66E-05	1.59E-04	⁷⁰ Ga	6.56E-10	2.11E-10	9.27E-11	1.24E-10
⁴⁰ K	5.99E-07	2.73E-08	1.35E-08	1.65E-08	⁷¹ Ga	1.99E-11	1.74E-10	7.51E-11	1.13E-10
⁴¹ K	9.58E-07	4.06E-08	2.05E-08	1.99E-08	⁷² Ga	9.93E-12	1.38E-10	5.53E-11	7.30E-11

Table 8—Continued

Models	A-1	B-1	B-2	B-3		A-1	B-1	B-2	B-3
⁴² K	1.79E-11	6.95E-11	3.91E-11	3.79E-11	⁷³ Ga	1.10E-11	1.52E-10	5.98E-11	8.06E-11
⁴³ K	7.21E-12	8.11E-11	4.19E-11	3.41E-11	⁶³ Ge	2.79E-05	1.48E-06	4.88E-07	1.60E-06
⁴⁴ K	4.45E-12	7.90E-11	3.84E-11	3.77E-11	⁶⁴ Ge	4.06E-02	1.69E-02	7.24E-03	1.05E-02
⁴⁵ K	4.16E-12	1.00E-10	3.78E-11	4.05E-11	⁶⁵ Ge	1.50E-04	7.10E-05	5.23E-05	4.21E-05
³⁸ Ca	1.42E-03	9.17E-05	3.61E-05	3.80E-05	⁶⁶ Ge	8.48E-03	5.55E-04	2.80E-04	3.00E-04
³⁹ Ca	3.00E-03	2.06E-04	7.89E-05	8.39E-05	⁶⁷ Ge	2.61E-04	1.18E-05	6.26E-06	5.58E-06
⁴⁰ Ca	7.03E-02	5.71E-01	3.59E-01	4.63E-01	⁶⁸ Ge	4.68E-02	1.98E-03	9.97E-04	9.52E-04
⁴¹ Ca	4.81E-05	3.77E-05	2.35E-05	3.64E-05	⁶⁹ Ge	2.27E-04	9.59E-06	4.84E-06	4.62E-06
⁴² Ca	8.38E-04	3.65E-05	1.84E-05	2.47E-05	⁷⁰ Ge	1.04E-03	4.38E-05	2.21E-05	2.11E-05
⁴³ Ca	1.55E-06	6.57E-08	3.37E-08	3.32E-08	⁷¹ Ge	8.96E-07	3.81E-08	1.92E-08	1.84E-08
⁴⁴ Ca	1.14E-06	4.81E-08	2.42E-08	2.33E-08	⁷² Ge	2.78E-08	1.41E-09	7.61E-10	6.81E-10
⁴⁵ Ca	6.55E-11	1.45E-10	5.04E-11	7.25E-11	⁷³ Ge	2.33E-11	1.63E-10	9.63E-11	8.29E-11
⁴⁶ Ca	5.62E-12	9.28E-11	5.45E-11	4.61E-11	⁷⁴ Ge	1.26E-11	1.53E-10	8.87E-11	8.11E-11
⁴⁷ Ca	4.46E-12	6.63E-11	3.61E-11	4.57E-11	⁷⁵ Ge	6.60E-12	1.63E-10	8.86E-11	5.69E-11
⁴⁸ Ca	4.01E-12	8.17E-11	4.34E-11	3.33E-11	⁶⁵ As	3.70E-09	1.69E-10	8.19E-11	8.45E-11
⁴⁰ Sc	8.98E-08	3.80E-09	1.91E-09	1.83E-09	⁶⁶ As	5.56E-07	1.83E-07	3.83E-08	5.49E-08
⁴¹ Sc	1.51E-04	6.64E-06	3.22E-06	3.16E-06	⁶⁷ As	3.99E-05	1.63E-05	5.84E-06	7.92E-06
⁴² Sc	2.13E-05	1.05E-06	4.67E-07	4.56E-07	⁶⁸ As	4.13E-06	9.82E-07	4.16E-07	4.04E-07
⁴³ Sc	1.43E-04	7.64E-06	3.29E-06	3.55E-06	⁶⁹ As	2.77E-06	1.80E-07	7.38E-08	7.03E-08
⁴⁴ Sc	1.56E-06	6.62E-08	3.34E-08	3.25E-08	⁷⁰ As	7.92E-07	3.38E-08	1.76E-08	1.63E-08
⁴⁵ Sc	8.43E-05	3.56E-06	1.87E-06	1.72E-06	⁷¹ As	1.87E-05	7.90E-07	3.99E-07	3.80E-07
⁴⁶ Sc	3.40E-08	1.53E-09	7.62E-10	7.26E-10	⁷² As	1.55E-07	6.74E-09	3.38E-09	3.25E-09
⁴⁷ Sc	1.45E-09	1.89E-10	7.61E-11	1.21E-10	⁷³ As	1.09E-07	4.92E-09	2.52E-09	2.37E-09
⁴⁸ Sc	5.61E-12	1.23E-10	4.45E-11	6.76E-11	⁷⁴ As	1.50E-10	1.38E-10	8.36E-11	9.52E-11
⁴⁹ Sc	5.77E-12	7.81E-11	5.26E-11	4.27E-11	⁷⁵ As	8.20E-11	2.17E-10	1.15E-10	1.39E-10
⁴² Ti	5.85E-04	2.46E-05	1.22E-05	1.18E-05	⁷⁶ As	8.53E-12	1.35E-10	5.92E-11	6.42E-11
⁴³ Ti	1.23E-04	6.28E-06	2.55E-06	2.96E-06	⁶⁷ Se	2.21E-08	9.79E-10	2.79E-10	3.95E-10
⁴⁴ Ti	1.28E-02	3.30E-03	1.60E-03	2.61E-03	⁶⁸ Se	2.86E-04	4.83E-05	1.55E-05	2.52E-05
⁴⁵ Ti	7.11E-05	2.69E-05	1.52E-05	1.20E-05	⁶⁹ Se	1.26E-06	3.68E-07	1.39E-07	2.36E-07
⁴⁶ Ti	1.16E-03	6.18E-05	3.25E-05	3.07E-05	⁷⁰ Se	1.24E-05	7.52E-07	3.38E-07	4.00E-07
⁴⁷ Ti	4.09E-06	1.86E-07	5.71E-07	9.57E-08	⁷¹ Se	1.00E-06	4.62E-08	2.26E-08	2.16E-08
⁴⁸ Ti	1.50E-05	6.32E-07	3.19E-07	3.05E-07	⁷² Se	7.15E-04	3.02E-05	1.52E-05	1.46E-05
⁴⁹ Ti	1.43E-08	7.22E-10	3.61E-10	3.65E-10	⁷³ Se	8.71E-06	3.68E-07	1.86E-07	1.77E-07
⁵⁰ Ti	3.54E-11	1.17E-10	5.98E-11	6.37E-11	⁷⁴ Se	1.48E-04	6.27E-06	3.16E-06	3.02E-06
⁵¹ Ti	4.88E-12	9.63E-11	3.21E-11	5.57E-11	⁷⁵ Se	9.18E-07	3.91E-08	1.98E-08	1.89E-08
⁴⁴ V	3.86E-04	1.65E-05	8.17E-06	7.89E-06	⁷⁶ Se	1.77E-06	7.64E-08	3.91E-08	3.69E-08
⁴⁵ V	1.57E-04	5.85E-05	1.29E-05	2.49E-05	⁷⁷ Se	2.21E-09	2.86E-10	1.28E-10	1.08E-10
⁴⁶ V	7.61E-05	1.86E-05	4.71E-06	6.83E-06	⁷⁸ Se	1.88E-10	2.45E-10	1.22E-10	1.04E-10
⁴⁷ V	8.10E-04	6.57E-05	2.59E-05	3.11E-05	⁶⁹ Br	4.76E-12	2.07E-13	1.03E-13	1.01E-13
⁴⁸ V	6.82E-05	2.94E-06	1.54E-06	1.47E-06	⁷⁰ Br	1.49E-09	1.15E-10	3.49E-11	4.13E-11
⁴⁹ V	2.86E-04	1.23E-05	7.88E-06	6.20E-06	⁷¹ Br	7.23E-07	4.28E-08	1.86E-08	1.93E-08
⁵⁰ V	9.02E-08	3.98E-09	2.00E-09	1.92E-09	⁷² Br	3.45E-08	3.46E-09	1.46E-09	1.89E-09
⁵¹ V	2.34E-07	1.00E-08	5.03E-09	4.87E-09	⁷³ Br	5.42E-08	1.07E-08	3.20E-09	5.88E-09
⁵² V	2.79E-11	8.86E-11	5.14E-11	6.41E-11	⁷⁴ Br	9.04E-09	1.78E-09	8.19E-10	8.46E-10
⁵³ V	7.36E-12	1.15E-10	5.36E-11	5.58E-11	⁷⁵ Br	2.73E-07	1.54E-08	7.13E-09	7.77E-09
⁴⁶ Cr	7.13E-04	3.69E-05	1.53E-05	1.68E-05	⁷⁶ Br	1.03E-07	5.96E-09	2.71E-09	2.93E-09

Table 8—Continued

Models	A-1	B-1	B-2	B-3		A-1	B-1	B-2	B-3
^{47}Cr	3.21E-04	4.92E-05	9.88E-06	2.15E-05	^{77}Br	1.14E-06	4.94E-08	2.50E-08	2.38E-08
^{48}Cr	1.70E-02	8.42E-03	4.31E-03	7.13E-03	^{78}Br	7.85E-09	1.31E-09	4.93E-10	7.45E-10
^{49}Cr	7.06E-04	3.71E-04	1.86E-04	2.60E-04	^{79}Br	6.43E-09	1.66E-09	1.12E-09	7.53E-10

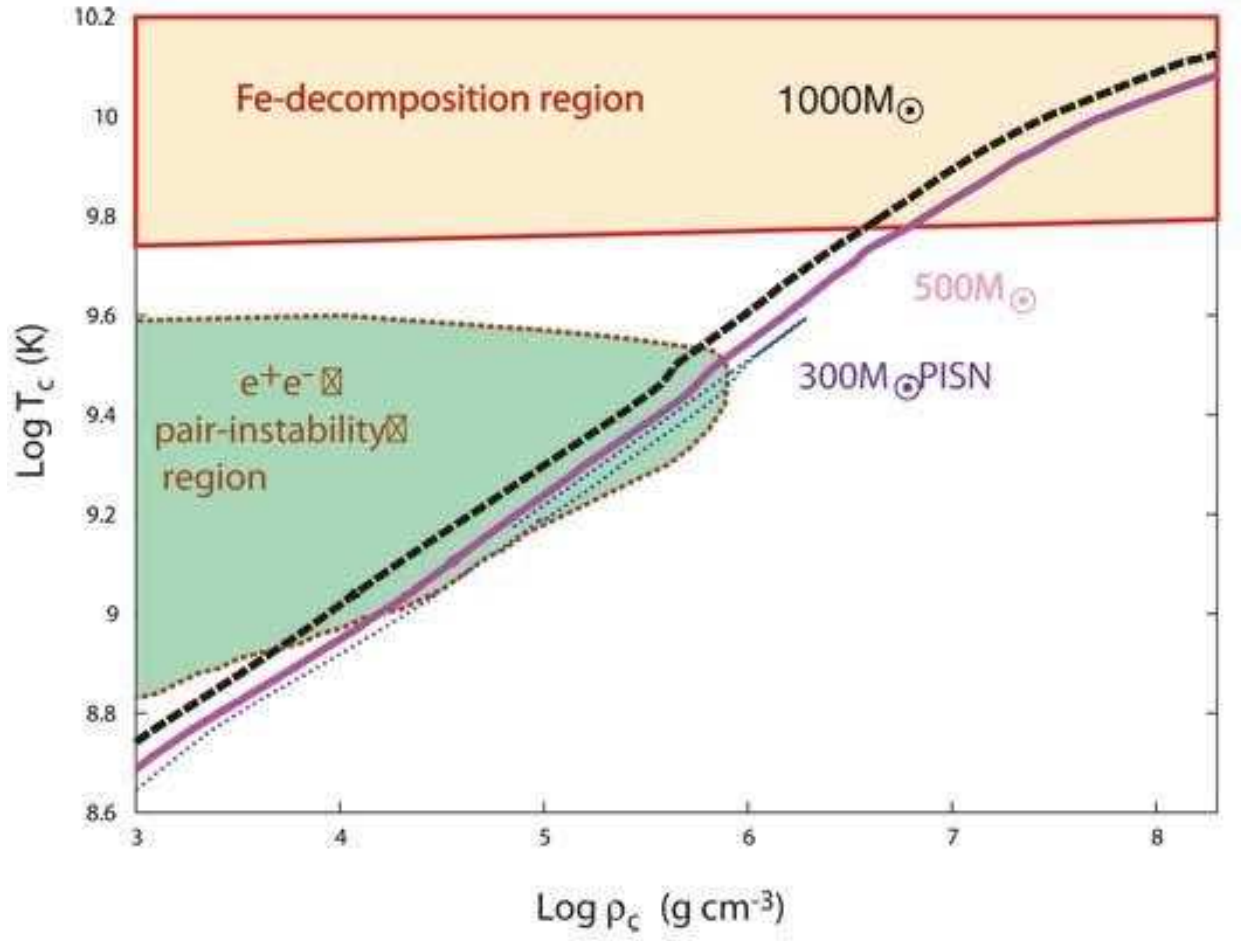


Fig. 1.— Evolutionary tracks of central temperature and density of the stars with $300 M_\odot$ (thin dotted line), $500 M_\odot$ (thick solid line), and $1000 M_\odot$ (thick dashed line).

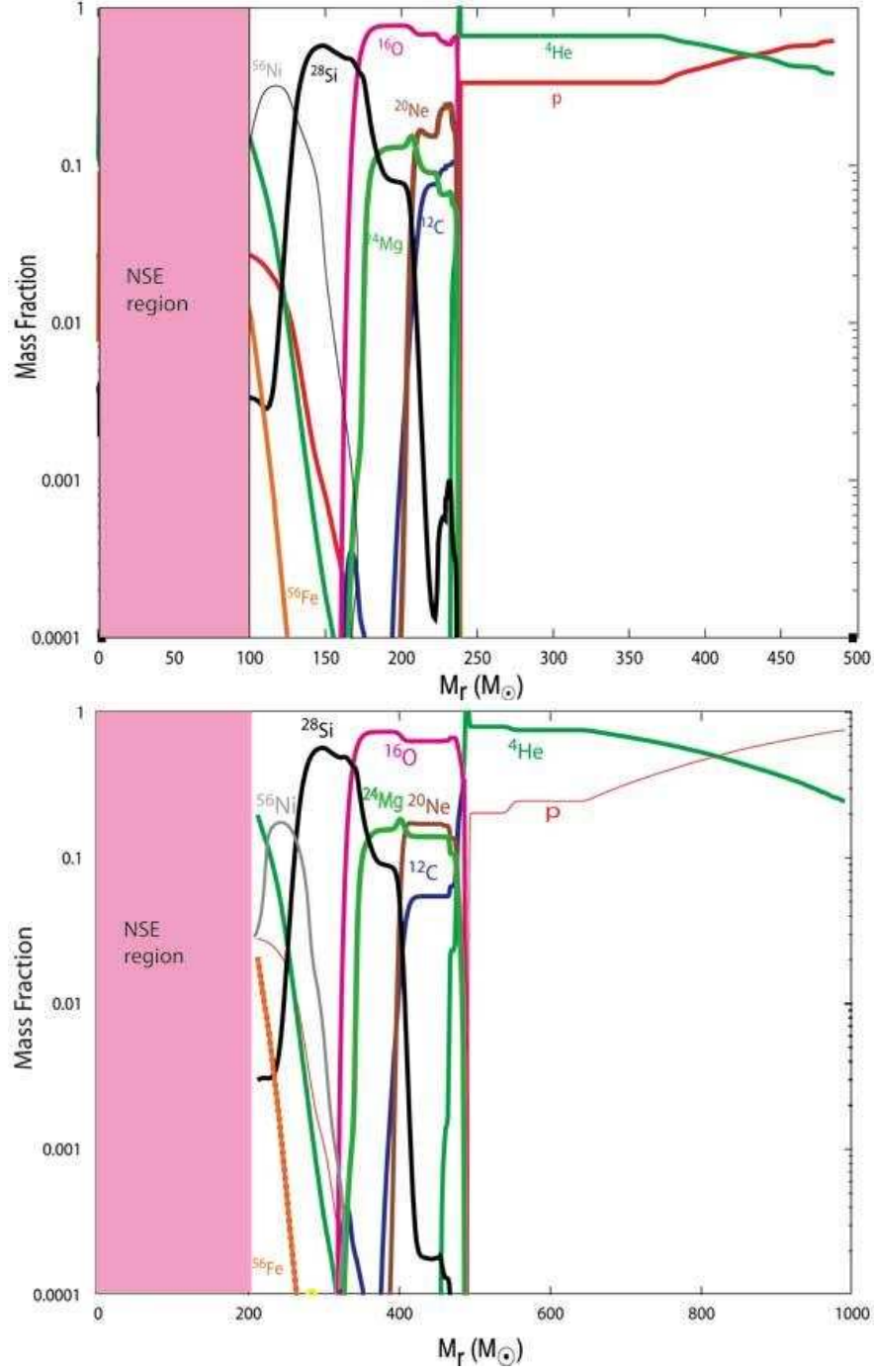


Fig. 2.— Chemical composition just before the explosion (when the central density reaches $10^{10} \text{ g cm}^{-3}$) of the $500M_\odot$ star (upper panel), and $1000M_\odot$ star (lower panel). The iron core occupies more than 20% of the total mass for both cases.

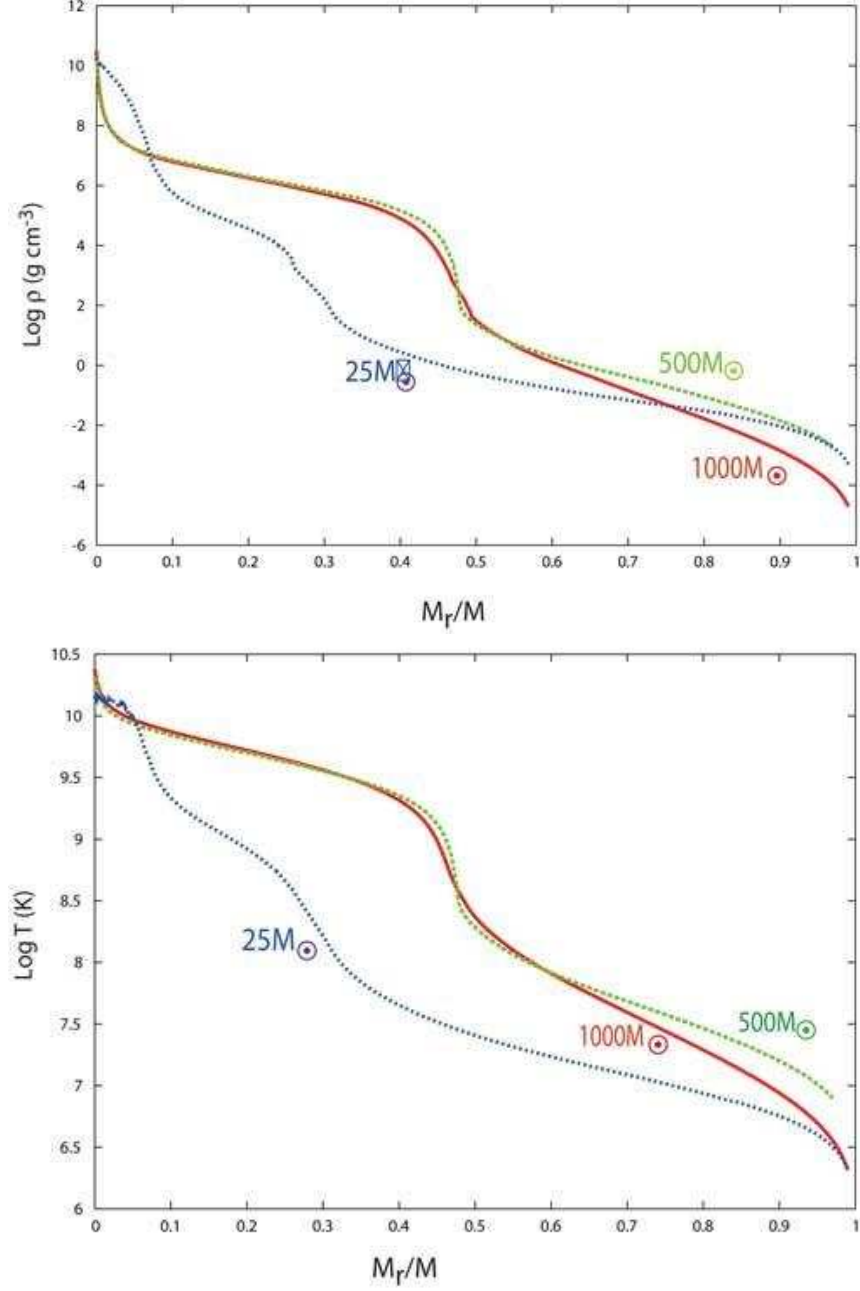


Fig. 3.— Density structure (top panel) and temperature structure (bottom panel) of $25M_\odot$, $500M_\odot$, $1000M_\odot$ models. The horizontal axis is the mass fractions M_r/M_{total} . The vertical axis shows the density (top), and the temperature (bottom), respectively. The data of $25M_\odot$ is from Umeda & Nomoto (2003).

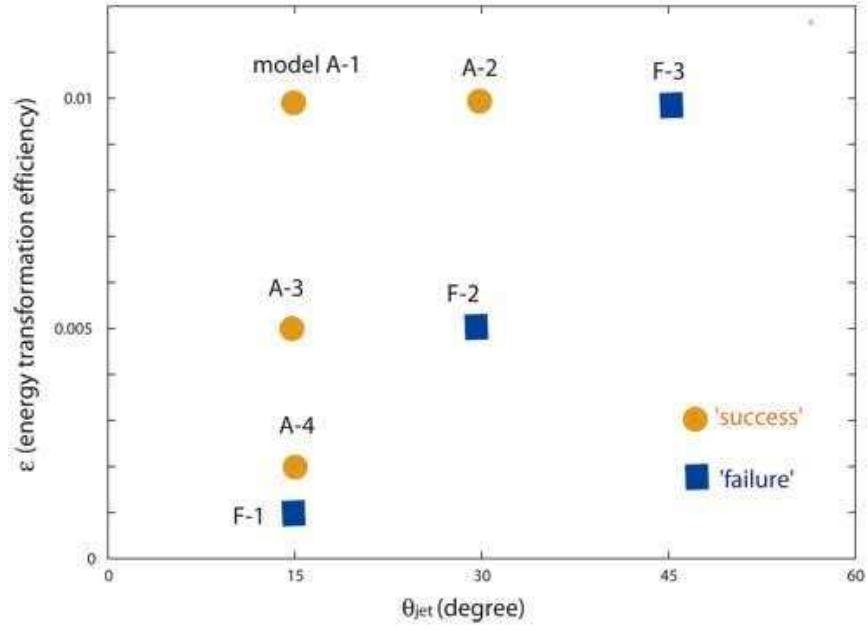


Fig. 4.— Models in which explosion occurs (filled circles) or not (filled squares), depending on two parameters θ_{jet} and ϵ for $1000M_{\odot}$ models. The other parameters are set at $\mu = 10\epsilon$, $M_{\text{BH}0} = 100M_{\odot}$, $f = 0.01$ (see Table 1, 2, and 5).

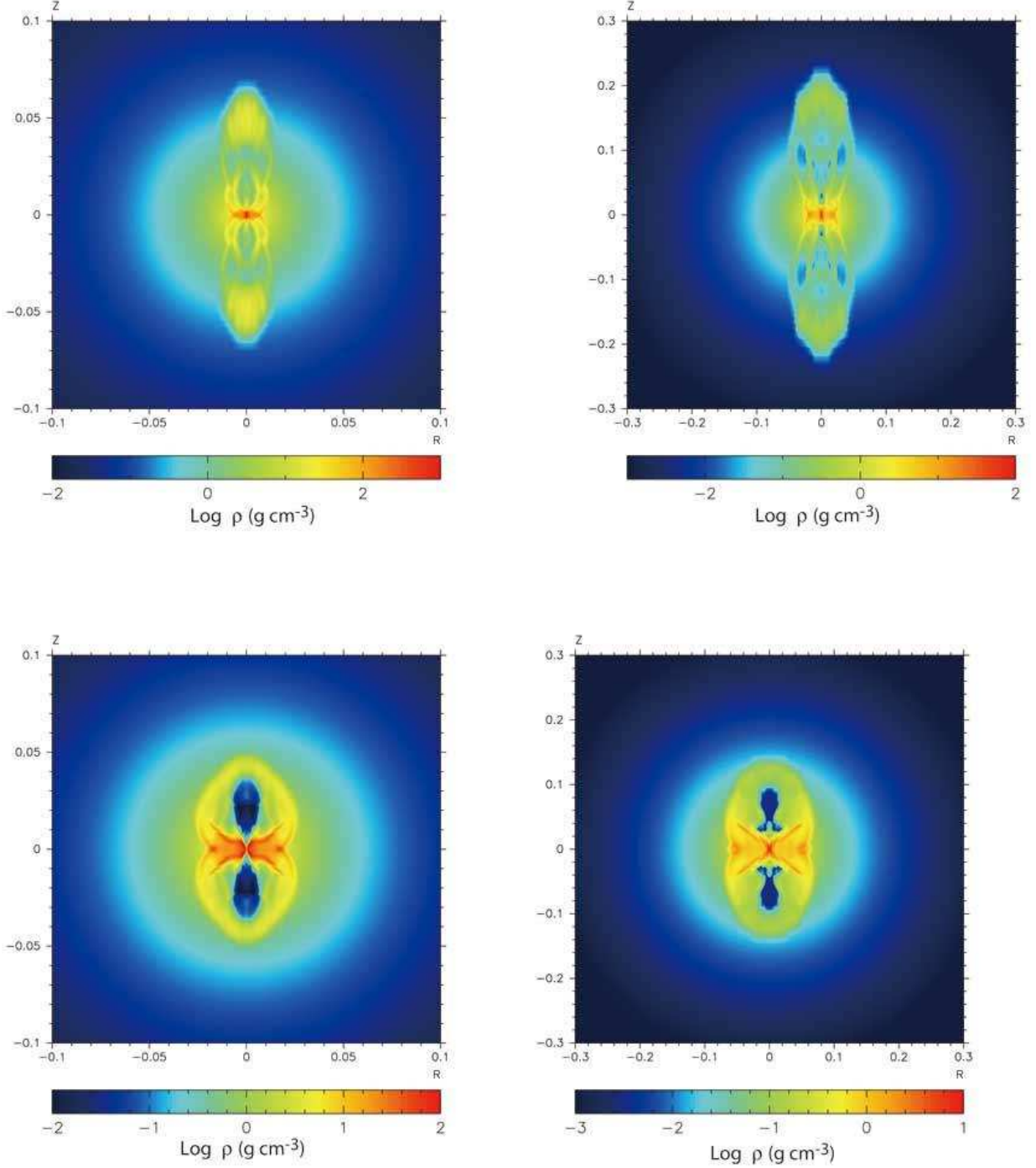


Fig. 5.— Snapshots of density structure showing how the jet is propagating at 30 second and 100 second after we started the calculation. The dial is normalized by the star’s radius ($\sim 7.7 \times 10^{12}$ cm). Note that θ_{jet} is set at 15° for both models. top left: 30s (A-1); top right: 100s (A-1); bottom left: 30s (B-1); bottom right: 100s (B-1).

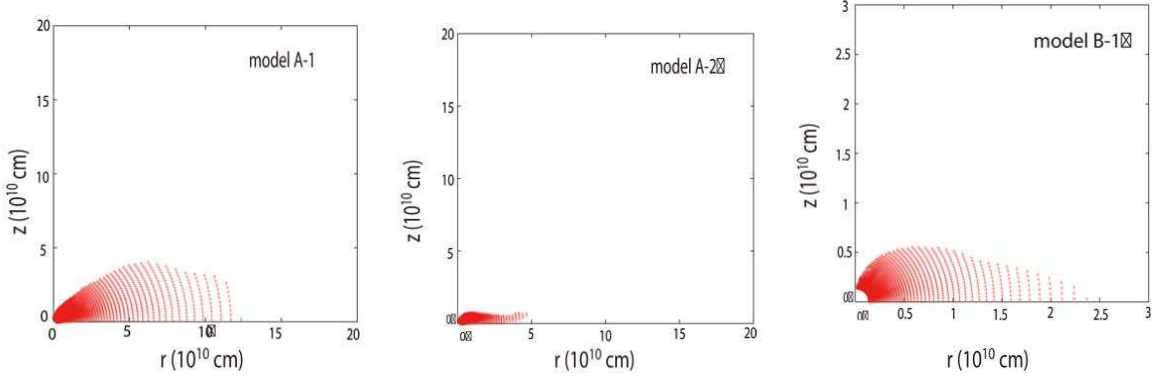


Fig. 6.— Initial radial positions of the matter that will be accreted into the central black hole for models A-1 (left), A-2 (middle), and B-1 (right). The blank region near the origin corresponds to the region of black hole initially formed.

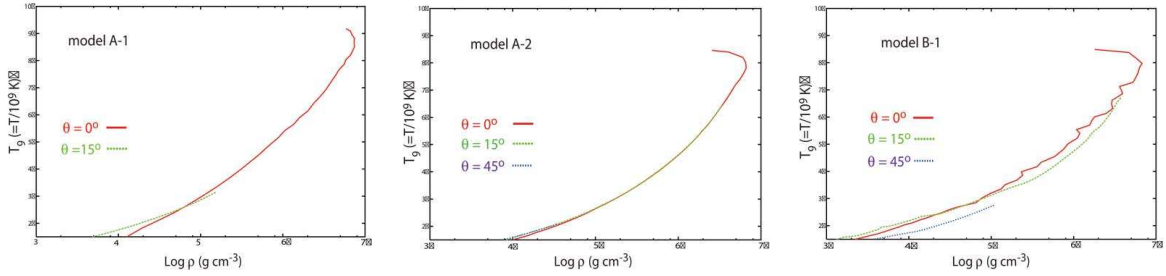


Fig. 7.— Maximum temperatures and densities of each mesh point for the directions of $\theta = 0^\circ$, $\theta = 15^\circ$, $\theta = 45^\circ$ for models A-1 (left), A-2 (middle), and B-1 (right).

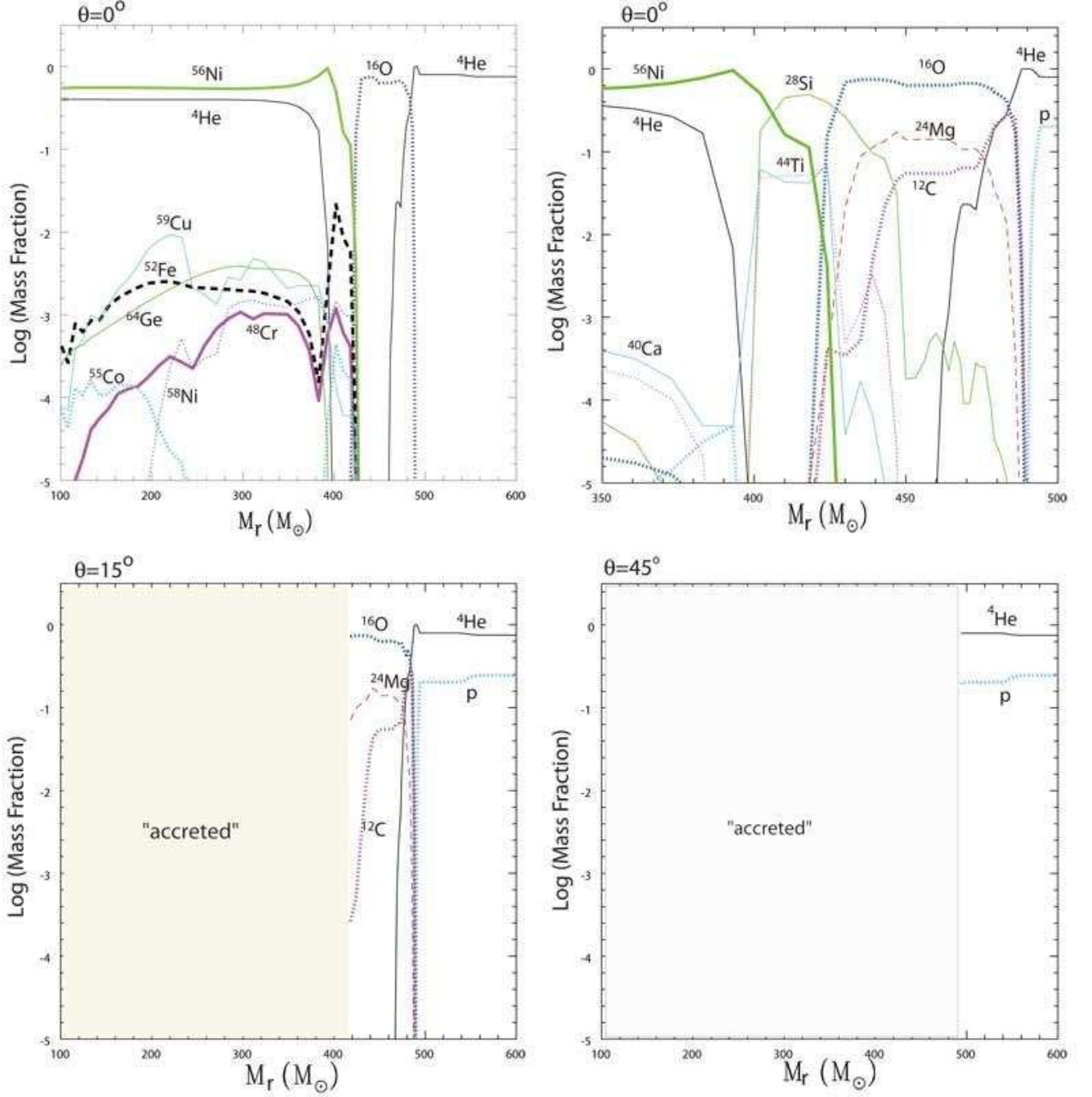


Fig. 8.— Distributions of elements: Fe-group elements for $\theta = 0^\circ$ (top left), α -elements for $\theta = 0^\circ$ (top right), α -elements for $\theta = 15^\circ$ (bottom left), α -elements for $\theta = 45^\circ$ (bottom right), for Model A-1. Note that the mass range is set to $350 - 500 M_\odot$ in the top right panel to see clearly the distributions of α -elements, while in others it is set to $100 - 600 M_\odot$.

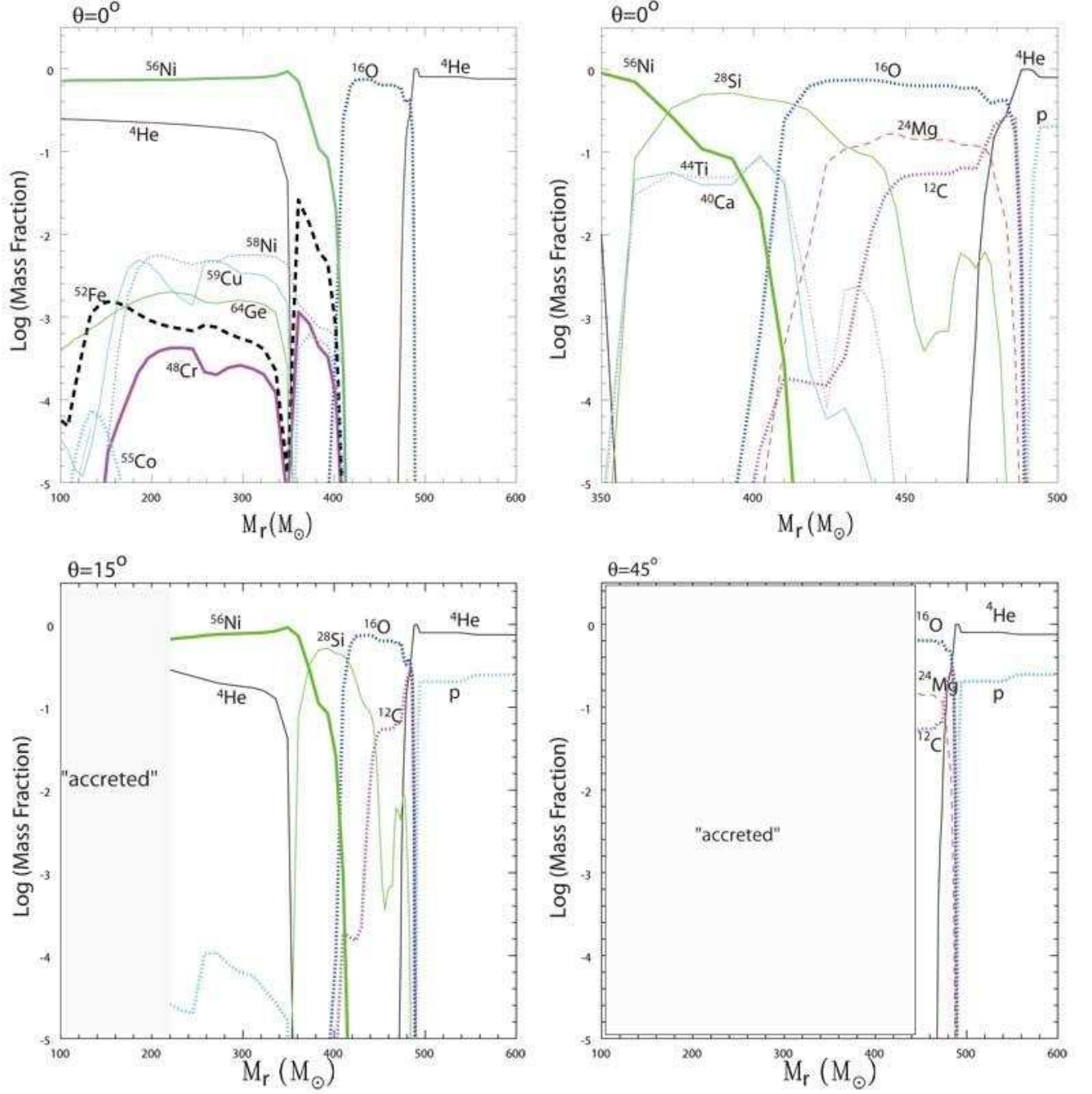


Fig. 9.— Same as Figure 8, but for Model A-2.

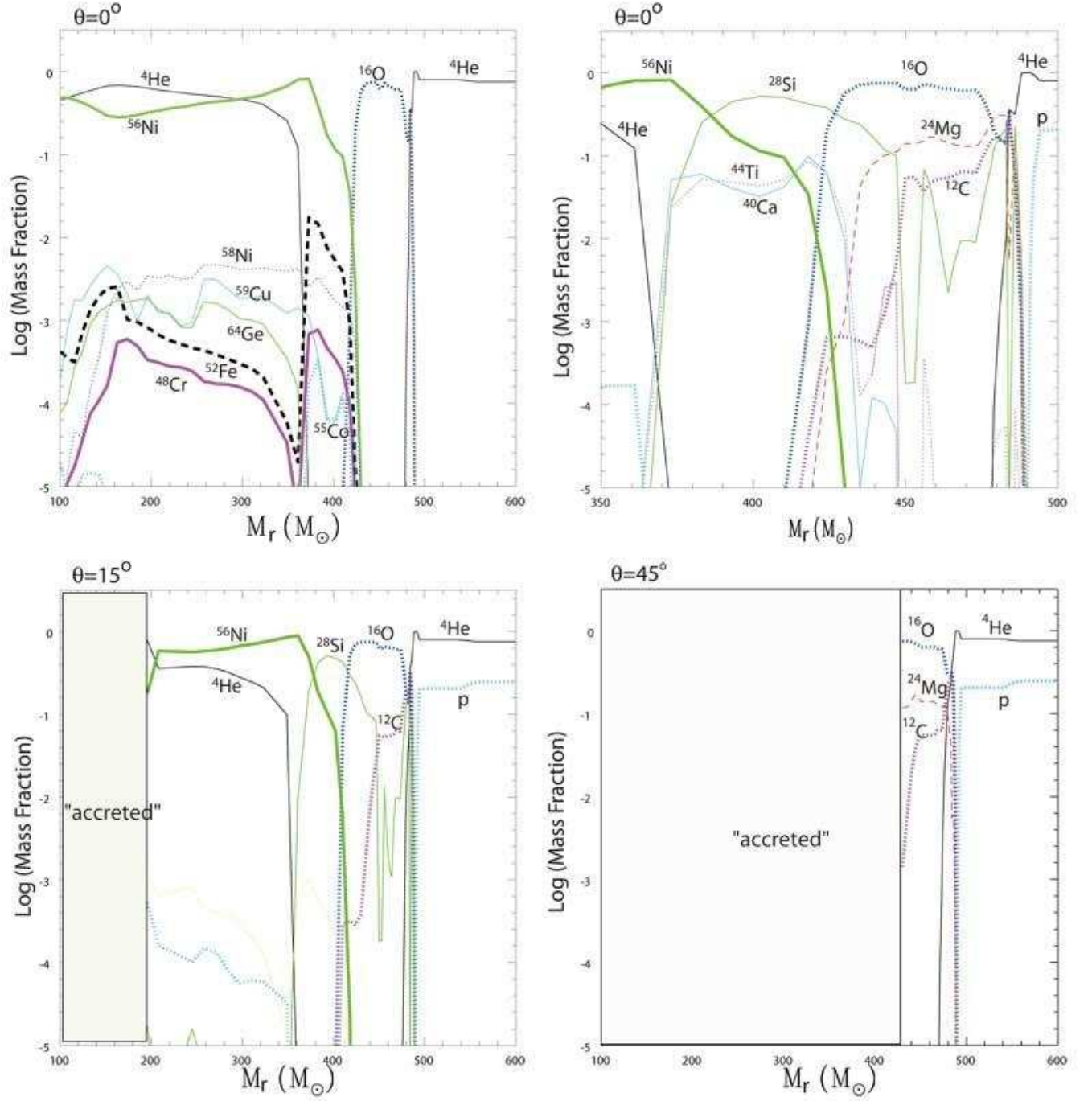


Fig. 10.— Same as Figure 8, but for Model B-1.

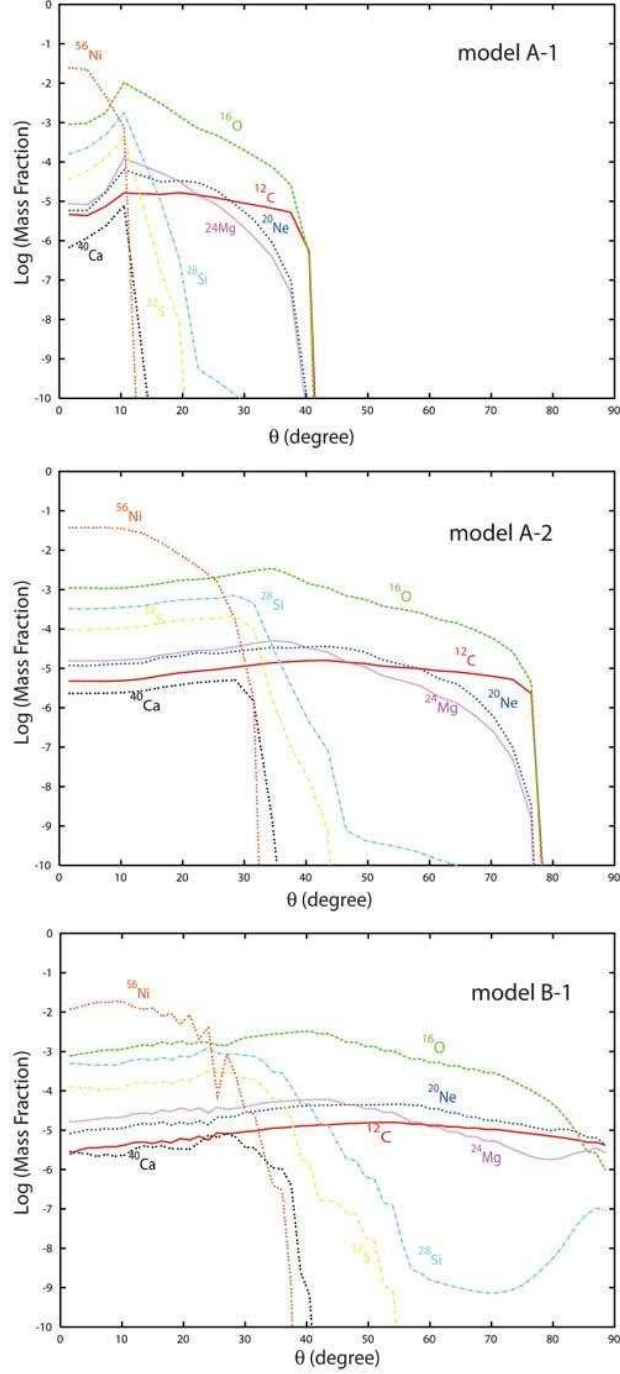


Fig. 11.— Mass fractions of ejected α - elements and ^{56}Ni as a function of the direction θ . These figures are for models A-1, A-2, and B-1. These values are obtained by integrating over radial direction for each θ .

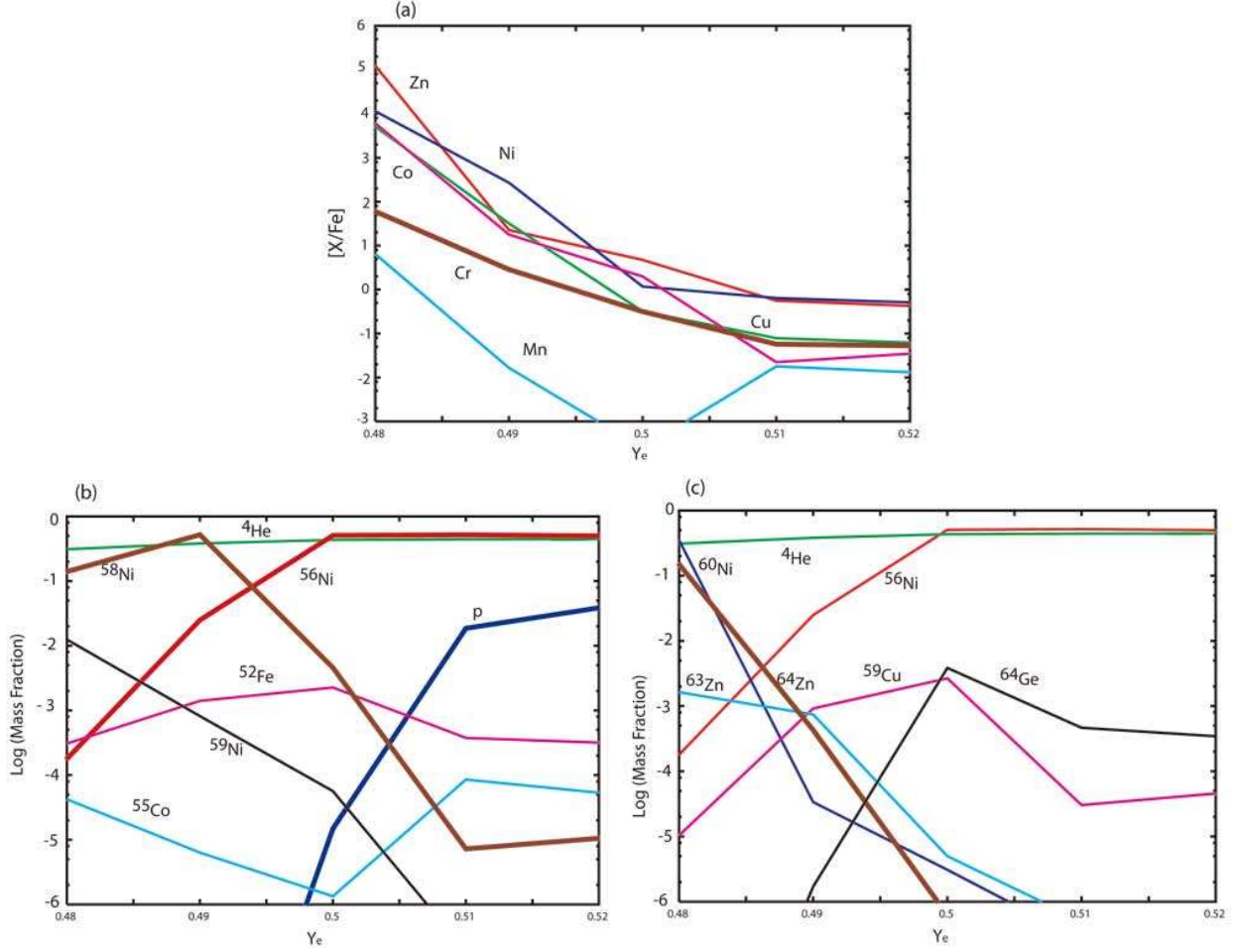


Fig. 12.— (a): $[X/Fe]$ for Fe-group elements as a function of Y_e for history A. (b), (c): Mass fractions of Fe-group elements, proton and ^4He as a function of Y_e for history A. Both (b) and (c) are for history A. Some different elements are shown separately in (b) and (c) for clarity.

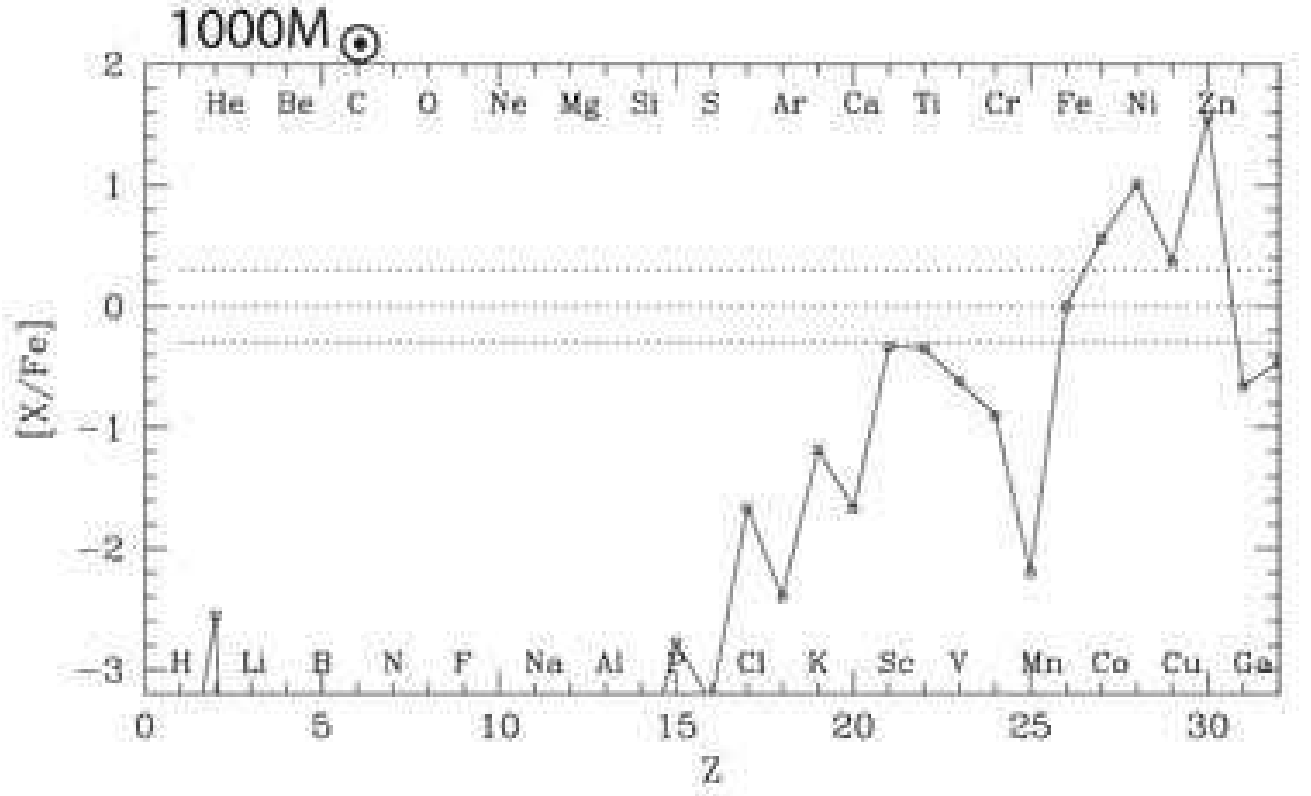


Fig. 13.— Abundance pattern of jet material averaged for 15 cases (5 Y_e values times 3 density-temperature histories).

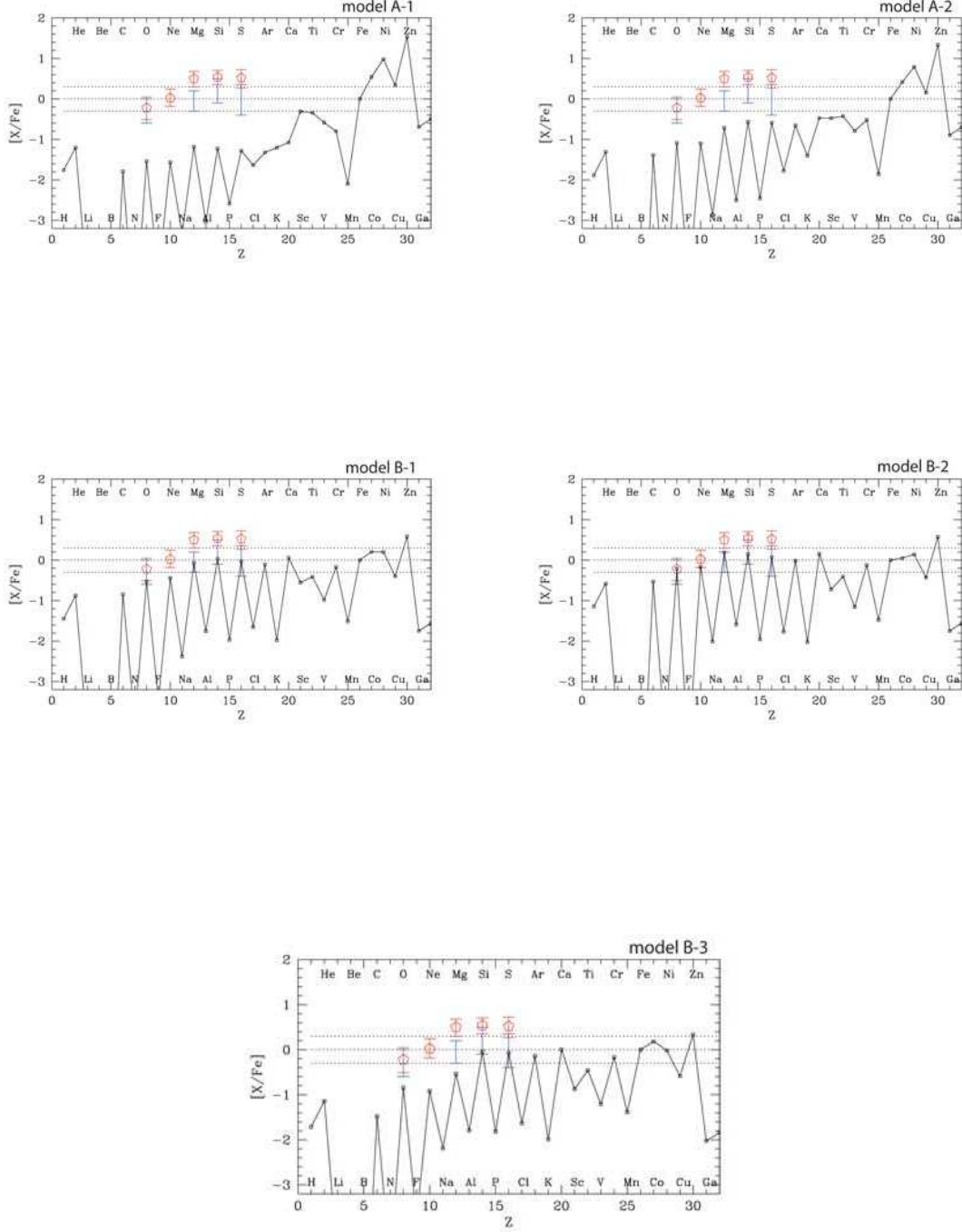


Fig. 14.— Total abundance patterns including jet contribution for higher resolution models. The open pentagons show the abundance ratios of gas of the central region in M82 (Ranalli et al. 2005). The bars show the range of abundance ratios observed in ICM (Baumgartner et al. 2004; Peterson et al. 2003).

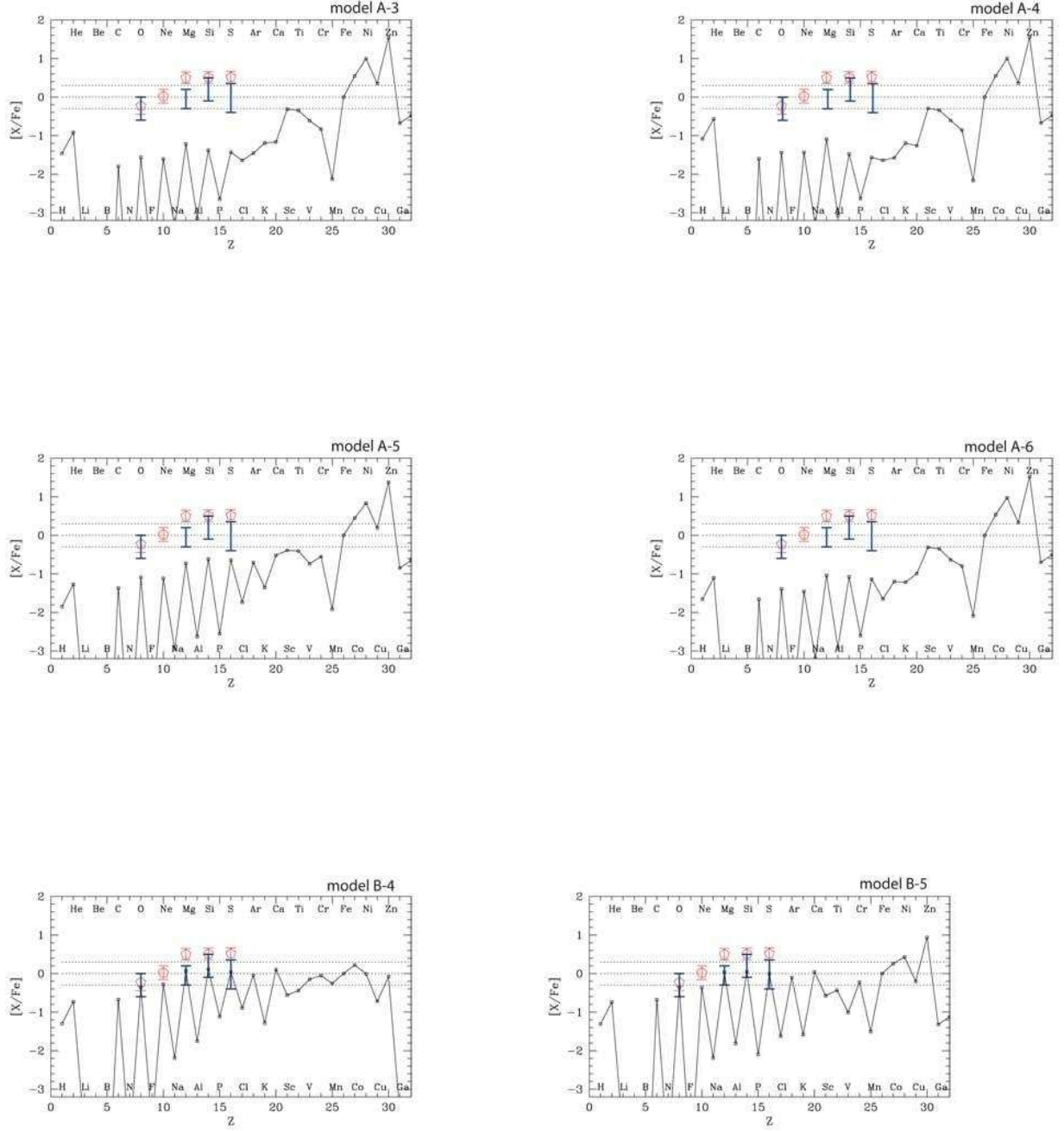


Fig. 15.— Same as Figure 14, but for lower resolution models.

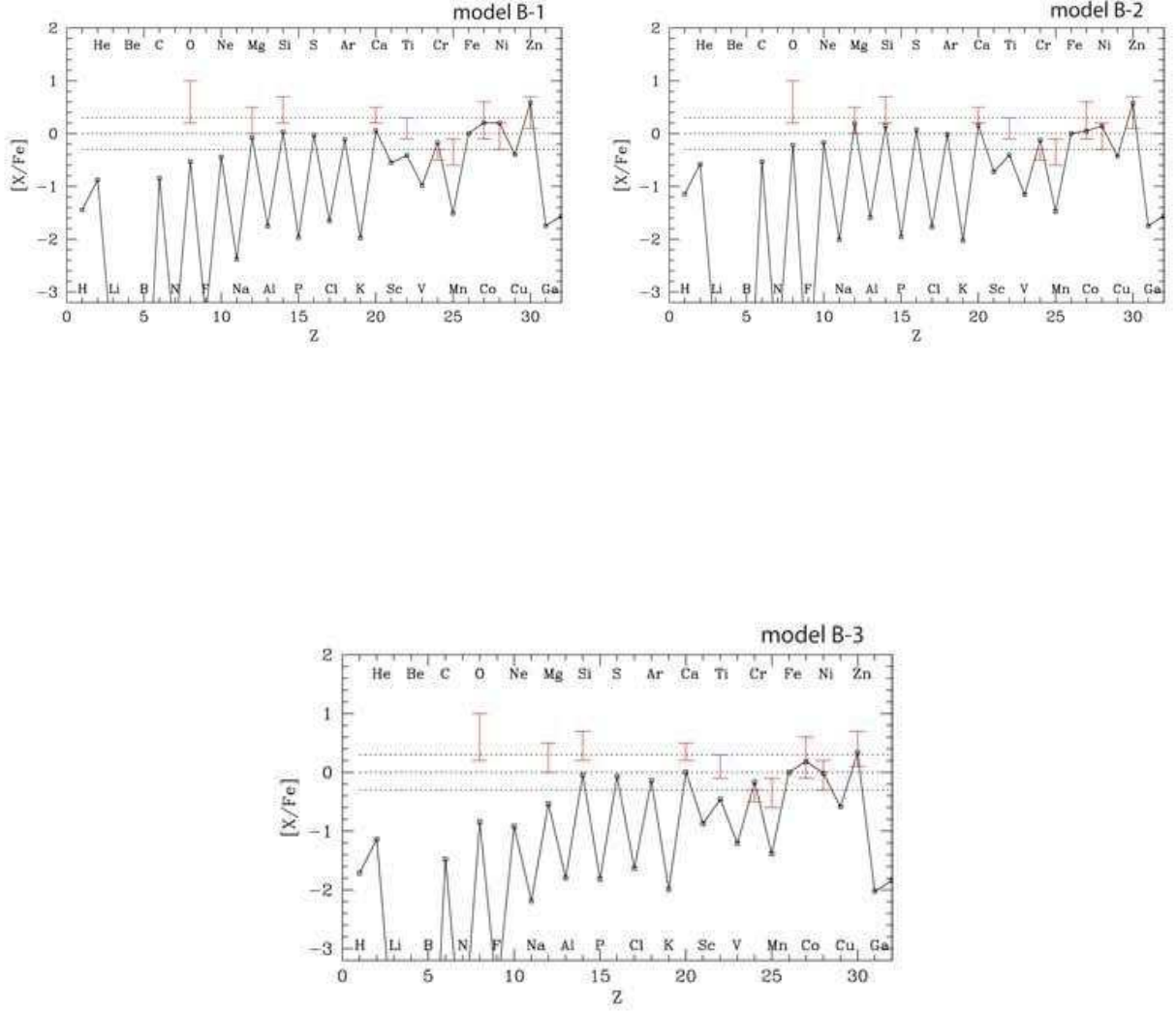


Fig. 16.— Total abundance patterns including jet contribution for Case B. The bars show the observational ranges of EMP stars' abundances in Galactic halo (Cayrel et al. 2004).